JOURNAL OF GEOPHYSICAL RESEARCH, VOL. 101, NO. A3, PAGES 5279–5297, MARCH 1, 1996

Plasma heating and flow in an auroral arc

T. E. Moore, M. O. Chandler, C. J. Pollock, and D. L. Reasoner[1]
Space Sciences Laboratory, Marshall Space Flight Center, Huntsville, Alabama

R. L. Arnoldy and B. Austin
Department of Physics, University of New Hampshire, Durham

P. M. Kintner and J. Bonnell
School of Electrical Engineering, Cornell University, Ithaca, New York

Abstract. We report direct observations of the three-dimensional velocity distribution of selected topside ionospheric ion species in an auroral context between 500 and 550 km altitude. We find heating transverse to the local magnetic field in the core plasma, with significant heating of O^+, He^+, and H^+, as well as tail heating events that occur independently of the core heating. The O^+ velocity distribution departs from bi-Maxwellian, at one point exhibiting an apparent ring-like shape. However, these observations are shown to be aliased within the auroral arc by temporal variations that are not well-resolved by the core plasma instrument. The dc electric field measurements reveal superthermal plasma drifts that are consistent with passage of the payload through a series of vortex structures or a larger scale circularly polarized hydromagnetic wave structure within the auroral arc. The dc electric field also shows that impulsive solitary structures, with a frequency spectrum in the ion cyclotron frequency range, occur in close correlation with the tail heating events. The drift and core heating observations lend support to the idea that core ion heating is driven at low altitudes by rapid convective motions imposed by the magnetosphere. Plasma wave emissions at ion frequencies and parallel heating of the low-energy electron plasma are observed in conjunction with this auroral form; however, the conditions are much more complex than those typically invoked in previous theoretical treatments of superthermal frictional heating. The observed ion heating within the arc clearly exceeds that expected from frictional heating for the light ion species H^+ and He^+, and the core distributions also contain hot transverse tails, indicating an anomalous transverse heat source.

Introduction

Auroral Ionospheric Upwelling

An extensive body of research exists documenting the outflow of ionospheric ions into the magnetosphere. This outflow occurs across the energy range from a fraction of an electron volt to several kilo electron volts, depending on the ion species involved, and the location from which the outflow is observed [*Yau and Lockwood*, 1988]. These outflows provide the dominant plasma within the inner magnetosphere [*Chappell et al.*, 1987; *Moore*, 1991] and are clearly of great significance in determining the characteristics of the magnetospheric plasma, perhaps influencing the timescales and locations of its dynamic processes by shaping the distribution of wave propagation speeds and current carrying capabilities.

[1]Deceased April 23, 1992

Paper number 95JA03154.
0148-0227/96/95JA-03154$05.00

Participation of heavy ions in the ionospheric source of magnetospheric plasma has been shown to be facilitated by, if not contingent upon, the dissipation of energy at relatively low altitudes in the topside ionosphere. While it is apparent that auroral plasma heating is distributed over a large altitude range [*Yau et al.*, 1983; *Moore et al.*; 1986a,b], it is also apparent that the characteristic energies achieved decrease with altitude continuously down to the F-region where Joule heating raises temperatures enough to drive observable upflows [*Loranc et al.*, 1990; *Tsunoda et al.*, 1989; *Wahlund and Opgenoorth*, 1989] but insufficiently to release the heavier ions from the gravitational potential of the Earth.

At some altitude in the topside ionosphere, processes occur which heat the heavy ions and perhaps electrons to characteristic energies of several electron volts, which is sufficient for the plasma to achieve scale heights comparable to the radius of the Earth, and thereby to become exposed to still more energetic processes including additional heating, acceleration by parallel electric fields, and high speed convective flows. Understanding the heating profile in the topside ionosphere is therefore a fundamental element in the development of an overall understanding of the magneto–sphere as the coupler of solar and terrestrial atmospheres.

Heating Mechanisms

The common thread running through virtually all ion heating measurements is the preferential transverse nature of the heating. Even when the heating appears in "ion conics" with peak flux oblique to the local magnetic field, one infers transverse heating at a lower altitude. In many other cases at low altitude, hot tail formation with flux peaking essentially perpendicular to the local field is widely observed [e.g., *Klumpar*, 1979; *Whalen et al.*, 1978; *Yau et al.*, 1983]. In other cases, the bulk characteristics of the plasma are inferred to incorporate a magnetically-aligned temperature anisotropy with the perpendicular temperatures in excess of parallel temperatures. [*Wahlund and Opgenoorth*, 1989; *Lockwood et al.*, 1987].

Transverse acceleration or heating quite clearly indicates that energization occurs by means of electric fields which are directed primarily perpendicular to the local magnetic field, as noted by *Sharp et al.* [1977]. However, considerable diversity exists in the description of the electric fields responsible for ionospheric transverse heating, with candidate fields ranging from DC convective fields [*St.-Maurice and Schunk*, 1979; *Barakat et al.*, 1983] through the ion cyclotron frequency range [*Ganguli and Palmadesso*, 1987], into the neighborhood of the lower hybrid resonance [*Chang and Coppi*, 1981; *Chang et al.*, 1986; *Crew and Chang*, 1990], and higher, including the suggestion that heating is produced by abrupt shock-like structures which appear impulsive in the ion frame, relative to ion gyro periods [*Lundin and Hultqvist*, 1989; *Newman*, 1990]. The sources of free energy proposed to power these waves range from the convection-driven ion ring-beam instability [*St.-Maurice and Schunk*, 1979; *Moore et al.*, 1986b], to the current-driven electrostatic ion cyclotron instability [*Lysak et al.*, 1980, *Ganguli and Palmadesso*, 1987], to the inhomogeneous energy density driven instability [*Ganguli et al.*, 1994]. Still more recently, *Arnoldy et al.* [1992] and *Kintner et al.* [1992] have presented evidence that intense, highly localized (50-100 m) lower hybrid solitary structures create hot tails in the topside ion transverse velocity distribution, proposing that the energy for such heating is derived from the ponderomotive collapse of pervasive auroral hiss waves [*Maggs*, 1978]. Typically, all these free energy sources are present to varying degrees in auroral situations characterized by intense and highly structured plasma motions.

Among the models of ionospheric heating, models of acceleration by strong DC electric fields make very striking predictions concerning the resulting observable phenomena [*Whealton and Woo*, 1971]. In particular, topside convection at superthermal velocities (larger than the local thermal speed) is predicted to result in the formation of ring or toroid-shaped ion distribution functions [*St.-Maurice and Schunk*, 1979] that have a significant minimum at the center of the core of the velocity distribution. Such ring distributions have been previously inferred to occur, based on RPA measurements [*St.-Maurice et al.*, 1976], and based on incoherent radar measurements [*Lockwood et al.*, 1987; *Lockwood and Fuller-Rowell*, 1987]. We report here in situ observations of the three dimensional distribution function of ionospheric ions that are apparently supportive of these earlier inferences, but in a much more complex situation including abundant other sources of free energy as well.

In the next section, we provide an observational overview, followed by an analysis of the observations. We then discuss the relationship among and implications of the observations and summarize the conclusions which can be drawn from them.

OBSERVATIONS

General

Observations reported herein were obtained from the fourth of a sounding rocket series known as Argon Release for Controlled Studies (ARCS-4). The payload was launched from Poker Flat Research Range, Chatanika, Alaska, into active auroral conditions at 0731 UT on 23 February 1991. It contained an instrument complement which measured energetic particles, electric field and waves, and core plasma composition. In addition, the payload supported an active experiment apparatus involving the operation of an argon ion beam source on a deployable subpayload. In other papers [*Pollock et al.*, 1992, 1995], we report the results of the experiment with ion beam operations. In the present paper we specifically avoid observations that could have been influenced by the ion beam, and focus instead on the three-dimensional ion composition measurements of the core of the ambient ion velocity distribution, the formation of superthermal tail distributions in ions, and upon correlated observations of the dc electric field.

The auroral context of this flight was documented by ground magnetometers, all-sky cameras, and scanning meridian photometers at both Poker Flat and Barter Island. During the period just prior to the launch, a bright and stable auroral arc formed well north of the launch site in a position under the predicted trajectory. This arc proved highly durable during the flight, and it showed only modest variability of brightness and position during the entire flight. A group of unsteady auroral forms was also present both prior to and during the flight, equatorward of the main arc. The meridian scan photometer data confirm that these arcs were very highly variable during the flight, to the extent that it is difficult to track individual forms from scan to scan of the photometer (16 s/scan at Poker, 80 s/scan at Barter Island). In contrast, the main arc maintained a clear identity which persisted for tens of minutes after the flight was over.

The ARCS-4 payload trajectory plane orientation was approximately centered between the local geographic and geomagnetic (centered dipole) meridians (geographic heading approximately 7.5° E, geomagnetic heading approximately 10° W). It reached an apogee of 620 km, and a downrange impact distance of 725 km. During the course of the flight the subpayload receded upward along the magnetic field direction, at a rate of 2.4 m/s. During the payload's traversal of the main auroral arc, the subpayload beam operations were having neglibible effects on the plasma ambient to the main instrumented payload, though plasma wave perturbations were observed there. In the sections below, we will refer all directions to an Earth-based coordinate system in which the Z axis is set parallel to the local magnetic field (downward), the X axis is set in the plane of the ARCS-4 trajectory and perpendicular to the local magnetic field, northward, and the Y axis completes an orthogonal triad, generally eastward (referred to as the BCC coordinate system).

Core Plasma

The scanning thermal ion composition spectrometer (STICS) was included in the ARCS-4 payload to provide detailed differential, three-dimensional ion velocity distributions by species in an auroral ionospheric context. The goal of this effort is to provide new insights into the processes responsible for the

heating of ionospheric plasma within the topside *F* region and its subsequent outflow into the magnetosphere through the auroral acceleration region. STICS differs fundamentally from earlier low-energy ion mass spectrometers in its differential energy response as well as its capability to scan its look direction. These capabilities permit a very different approach to data analysis in which count rates may be interpreted directly as phase space densities, given a knowledge of the spacecraft floating potential relative to the plasma. In the auroral ionosphere where the spacecraft floats negative and positively charged ions are accelerated as they approach the payload, the STICS data provide a useful measure of the floating potential (see below).

A more complete description of the STICS instrument is being prepared for publication in *Reviews of Scientific Instruments*. The following brief description will serve for present purposes. STICS consists of the following major components: an aperture containing electrostatic deflection plates for selection of arrival angle; an electrostatic focussing mirror for definition of a differential energy passband; a conventional magnetic sector mass/charge analyzer equipped for simultaneous detection of two species in a mass/charge ratio of 4:1; associated stepping power supplies, preamplifiers, counters, and a programmable sequencer which stores and executes the flight power supply sweep program. A brief summary of STICS operational specifications is given in Table 1.

Figure 1 provides a spectrogram overview of the ARCS-4 rocket flight from the perspective of the O^+ plasma sampled along its trajectory. In the upper panel we see that the plasma occupied only a fraction of the energy range, which was extended to make possible observations of the argon ion beam generated on the deployed subpayload (nominally 100-eV and 200-eV operations). The elevated O^+ energies indicated at the very beginning of the spectrogram resulted from the operation of the argon beam in close proximity to the diagnostic payload, but no measurable O^+ response to the beam operations was recorded after the subpayload had moved away beyond a few tens of meters. Quite the contrary is true of the ambient H^+ plasma, which was transversely heated by operations of the Argon beam to a degree which was measurable throughout the first half of the flight [*Pollock et al.*, 1992, 1995]. It can be seen that the energy extent of the O^+ count rates is larger near the beginning and toward the end of the flight than in the middle. This is the signature of the relatively large ram velocities (up to 3 km/s) present during ascent and descent of the payload through the *F* region, rather than being indicative of heating. The feature of primary interest here is the period of elevated energies recorded between approximately 570 to 605 s time after launch (TAL). This is the period of passage through the bright poleward auroral arc.

The derivation of velocity distributions and three-dimensional moment parameters from the STICS count rates requires a complete specification of the attitude of the payload during its spinning motion. This is a distinctly nontrivial matter that has required a significant effort to complete. Two independent derivations of the payload attitude have been determined from the onboard aspect magnetometer and horizon sensor, and the two have been reconciled to validate the attitude solution. At this time there is a high degree of confidence in the qualitative and quantitative accuracy of the attitude knowledge (at the level of 1 deg. error bars).

The lower panels of Figure 1 show the signatures of payload motion through the O^+ plasma. The pitch angle spectrogram shows the upward and then downward motion of the payload, while the azimuth spectrogram shows the ram motion of the payload in the direction perpendicular to the local magnetic field. Pitch angle is defined here with respect to the downward direction along the local magnetic field, so that plasma appears to be downgoing at small pitch angles during the ascent, and vice versa during descent. Azimuth angle is defined with respect to the *X* direction (along the trajectory, essentially magnetic north), so that the peak plasma flux appears at southgoing azimuths. A distinct reduction of the Mach number (reduction of the ratio of ram to wake flux within a single time "stripe") can be seen around 280 s TAL, a weak crosswind toward the west (flux peak moving toward the west) can be seen persisting from 280 s through arrival at the auroral arc, and a strong crosswind is noticeable as the payload passes into the auroral heating event. These features are treated in a quantitative way below.

As shown in Figure 2, the H^+ (and He^+) plasma exhibits much smaller Mach number (smaller ratio of ram to wake flux) owing to its relatively large thermal speeds (compared with the payload speed). Coupled with the lower count rates for H^+ as a minor species, this renders H^+ (and to a lesser extent He^+) much less useful as a measure of the bulk plasma motions of the magnitude experienced in this flight. The errors associated with counting noise and Mach number are discussed more quantitatively in the appendix.

Table 1. ARCS-4/STICS Operational Specifications

Item	Specification
Angle scan range/resolution	±70° / 10°
Energy range/resolution	0.5 to 200 eV / 22%
Mass range/resolution	m/q = 1, 4, 8 / 30%; 4, 16, 40 / 5%
Effective area	1.5×10^{-2} cm^2 (at 10 eV, nominal FOV)
Solid angle of response	3×10^{-2} ster (10° x 10° at nominal FOV)
Basic sampling period	1.0 ms
Pitch angle sweep period	32 ms
Energy/angle sweep period	896 ms
Mass step period	1.792 s
Spin period	1.715 s
Spin/sweep beat period	12 s

Magnetospheric Plasma

ARCS-4 was equipped with energetic particle electrostatic analyzers covering the full range of pitch angles (by use of capped-hemispherical analyzers and imaging detector systems) and the energy range from 10 eV to 20 keV. These detectors documented the overflight of an intense evening auroral arc in coincidence with the plasma heating seen in the spectrograms above.

Figure 3 is an energy spectrogram of the energetic electron energy flux measurements centered at 0° pitch angle (downcoming), acquired as ARCS-4 passed over the stable poleward arc. It can be clearly seen that the electron population exhibited the classic signature of a "monoenergetic peak" [*Evans*, 1974], which is nearly isotropic over the downgoing hemisphere [*Arnoldy et al.*, 1985]. In addition, the spectrogram shows that

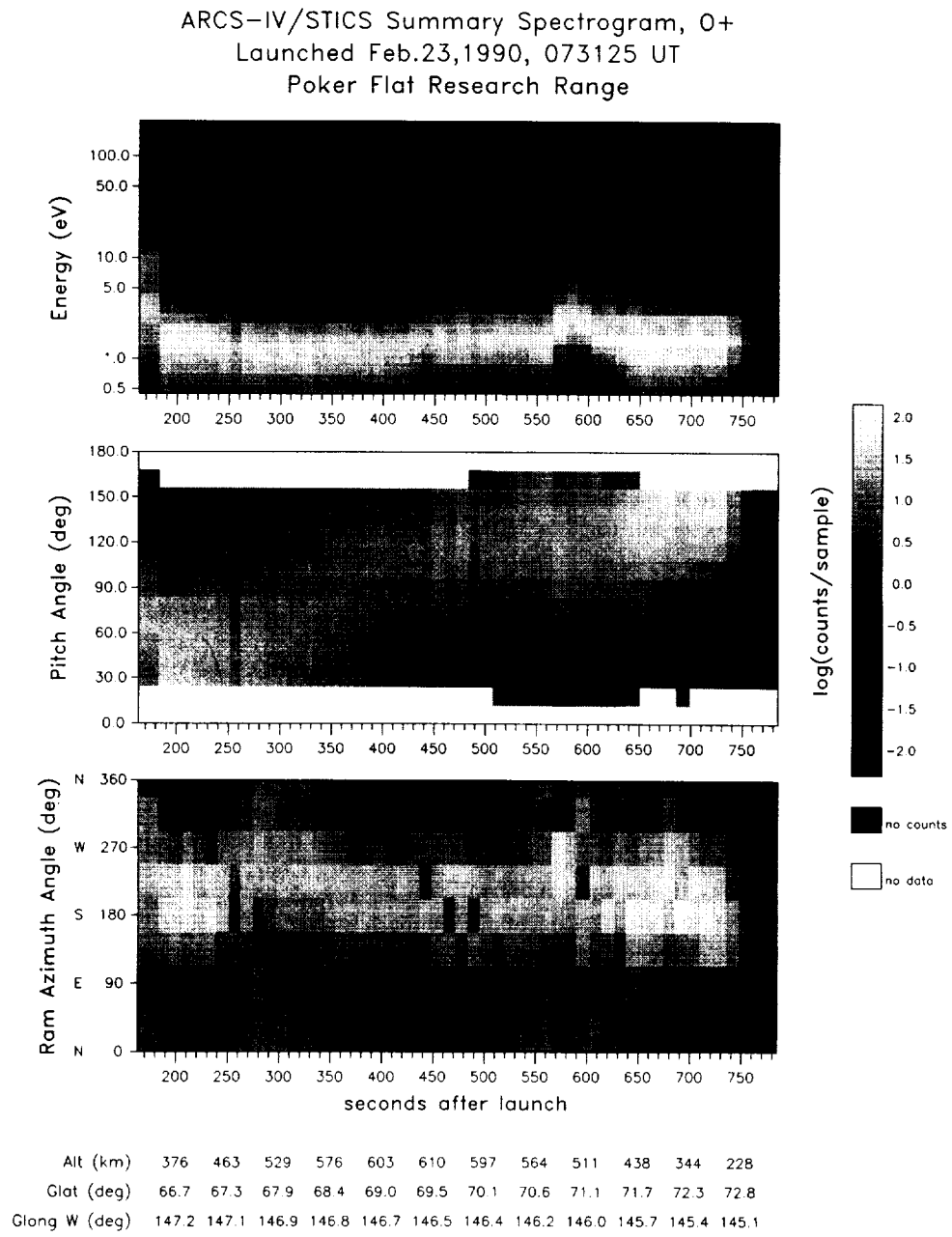

Figure 1. Energy, pitch, and azimuth spectrograms for O^+ ions observed at the ARCS4 main payload. Position data is indicated along the time axis. The quantity plotted is summed over the complementary two of the three velocity space variables for each panel.

enhanced energy fluxes existed within the arc at the very lowest energies sampled.

Owing to detector saturation of angular imaging, it cannot be said if field alignment was or was not present in the lowest energy measured electron fluxes (~50 eV). However, the electrons in the 200 eV and higher energy ranges were not affected by imaging saturation and were definitely field-aligned. The electron fluxes shown in Figure 3 are downcoming parallel fluxes. Upgoing fluxes were not sampled but could have been present at the same times. The enhancement of parallel low energy electron flux was present throughout the auroral arc, not solely associated with its edges. It therefore appears clear that these electrons represent a hot parallel tail on the thermal electron core. There is considerable detail in the low energy electrons, including energy dispersive features. These were among the subjects of a paper by *Lynch et al.* [1994], and we will not dwell on them here.

Fields and Waves

ARCS-4 was equipped with a single set of 5.5-m (tip to tip) Weitzmann boom electrostatic probe systems, mounted orthogonal to the cylindrical payload (spin) axis. A second probe system was deployed along the spin axis upward from the payload. The low-frequency difference potentials (i.e., dc electric fields) and their fluctuations on these probes were recorded by

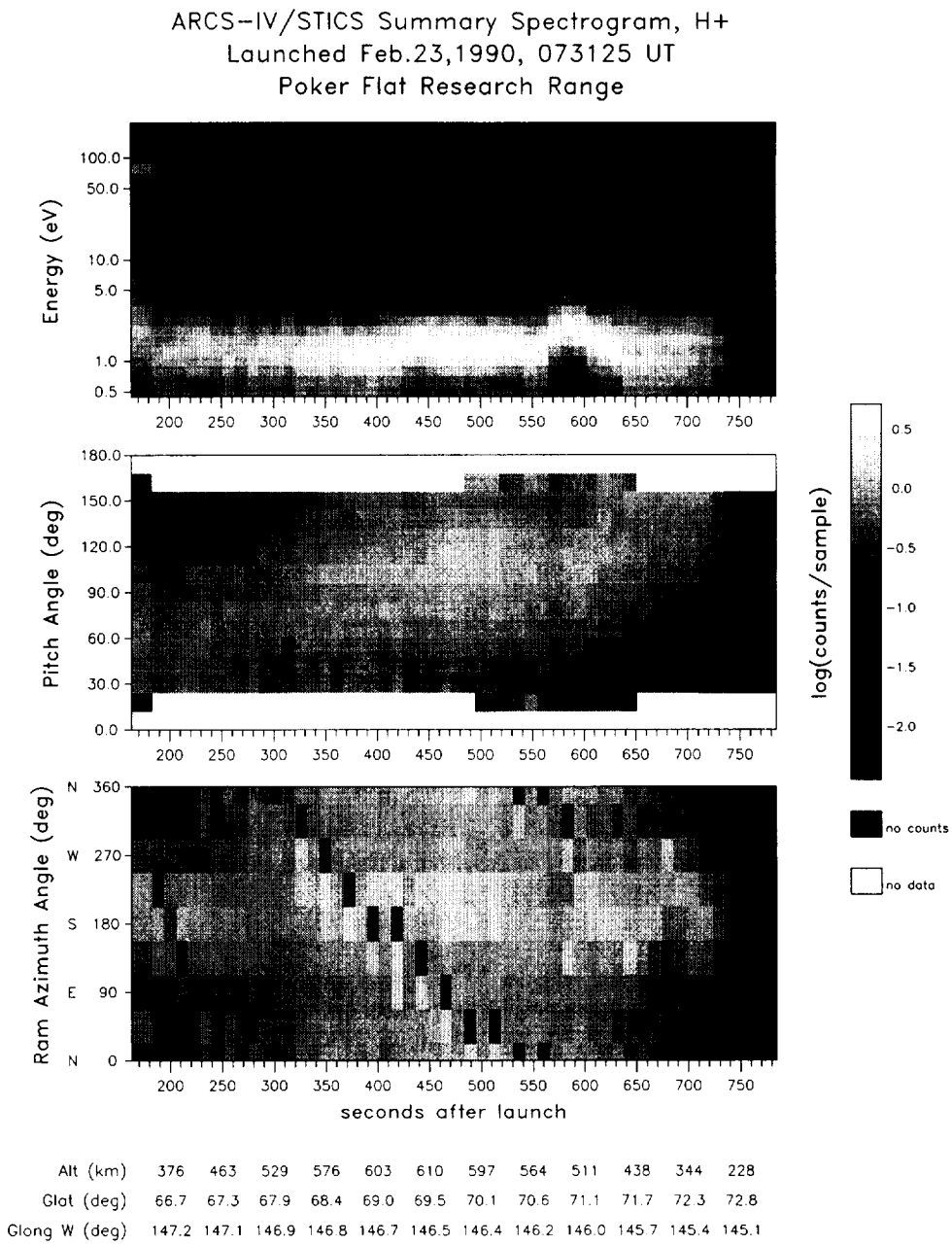

Figure 2. Similar to Figure 1., but for H^+ ions.

digital sampling over the range from dc up to 16 kHz using a dedicated video FM-FM data link, and by a swept frequency receiver over the range up to 5 MHz. In addition, the tip-to-tip probe potential and the probe-payload potential differences were separately digitized and telemetered at a resolution of 10 bits, with 256 samples per s.

Figure 4 shows the raw dc electric field (DCE) waveform caused by payload spin for a time period that begins prior to entry into the main auroral arc, spanning the arc traversal, and continuing for a period beyond the bright part of the arc. The wave form is clean and sinusoidal prior to entry into the arc. It begins to show increased magnitude and variations associated with the arc beginning at 570 s TAL, contining until ~605 s TAL. These variations consist of two main types: first, there are large variations in the phase and amplitude of the "sinusoidal" signal; second, there are several impulsive higher frequency disturbances of the waveform that may be identified as solitary structures [*Kintner et al.*, 1992]. However, in this case, the frequency bandwidth of these solitary structures was limited to several hundred Hertz instead of extending well above the lower hybrid resonance [*Vago et al.*, 1992]. A number of such structures occur during the traversal of the arc, within the strong DCE variations. A second burst of solitary structures occurs between 640 and 670 s TAL, apparently unassociated with the primary auroral precipitation or the strong DCE variatons. An analysis of the electric field data is presented in the Analysis section below.

Figure 5 is a spectrogram of the swept frequency receiver data showing the plasma frequency line and its variations during the flight, as well as the interpretation in terms of electron density. We note the general trend which is consistent with the motion of

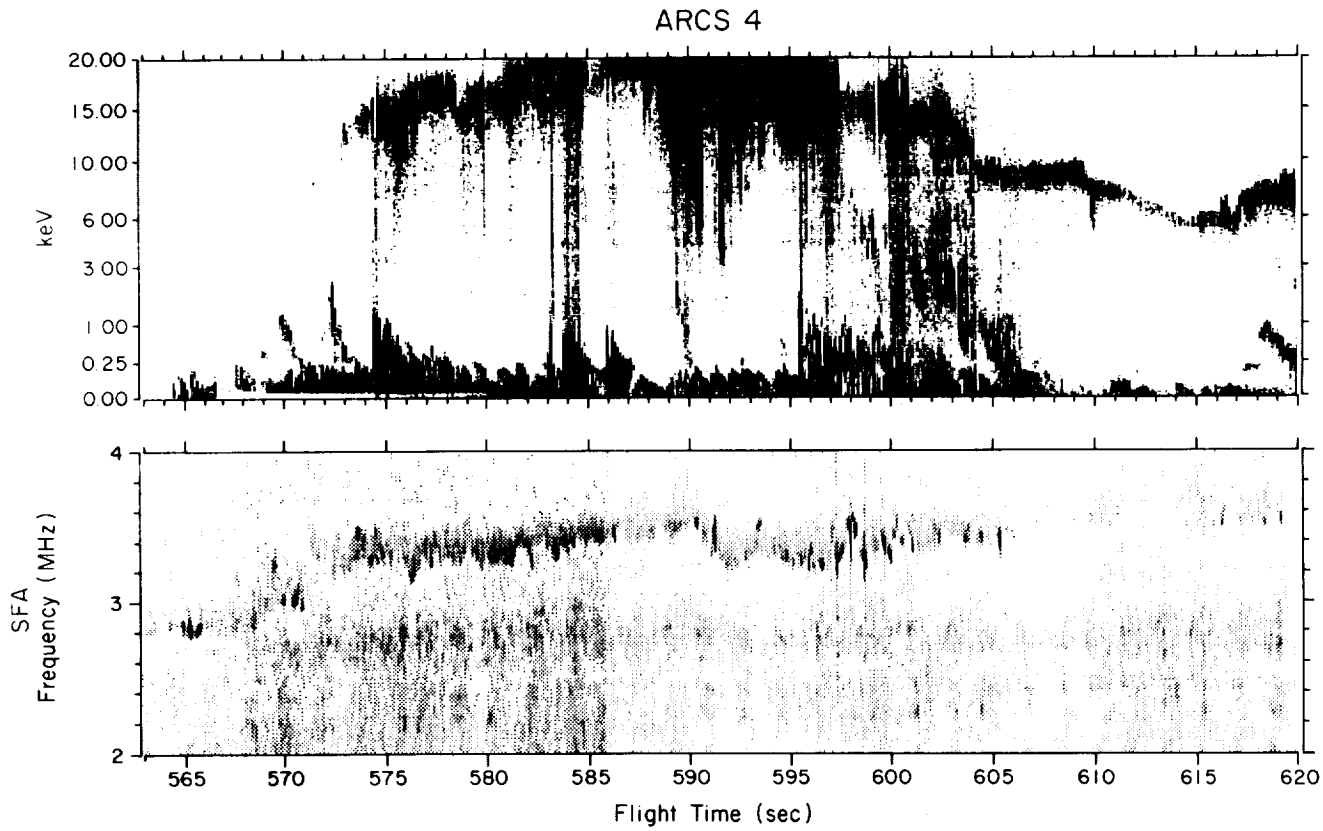

Figure 3. Energy spectrogram of energetic electron energy flux observed during the ARCS4 flight as the payload overflew the bright auroral arc. In addition to the intense feature at high energy, a notable set of features is seen at the lowest energies, below ~250 eV.

the payload upward through the topside *F* region, with an electron density scale height of 240 km in the altitude range sampled.

Spectrograms of the broadband receiver 0-16 kHz fluctutation amplitudes during this flight [*Pollock et al.*, 1995] exhibit pervasive auroral hiss emissions with a cutoff at the lower hybrid resonance, as well as broadband and harmonic emissions produced by the operation of the ion beam on the remote subpayload, with duty cycle consisting of 10 s on, 10 s. off, and alternating operations at 100 eV and 200 eV. As noted above, these waves did not produce a signature in the ambient O^+ plasma at the main diagnostic payload and are not of apparent relevance with respect to the auroral core plasma heating. However, owing to the variable wave emissions from the subpayload and the responsive changes in the broadband receiver gain control, it is not possible to accurately determine the variations which may have occured in the background or natural auroral hiss, in connection with the auroral arc.

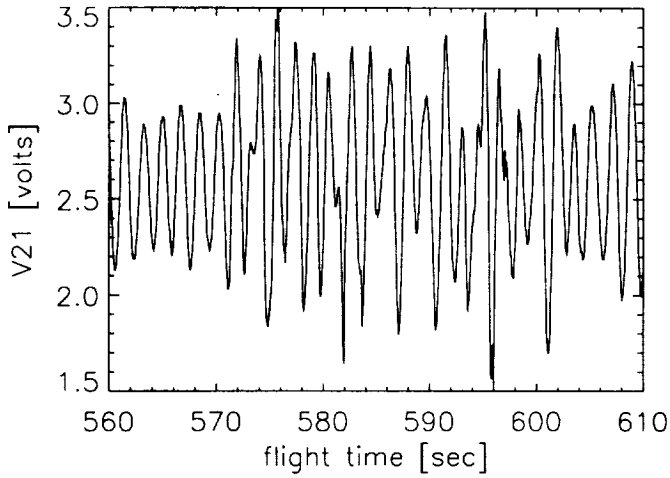

Figure 4. Raw dc electric field waveform, in telemetry units proportional to the interprobe potential, for the period indicated.

Tail Heating

The ARCS-4 payload also contained a set of hemispherical electrostatic energy and pitch angle spectrometers (HEEPS), configured so as to sample ions without mass analysis over the range from 0 to 950 eV. These analyzers continuously sampled the full pitch angle range in 64 angular sectors and scanned in azimuth with payload spin. Their response in energy was swept exponentially over this range in 32 steps once every 0.256 s. This instrument was designed to monitor the hot tail of the core plasma distribution.

Transverse hot tail formation was observed by the low-energy ion HEEPS, primarily in the regions where solitary structures were seen in the dc electric field. In Figure 6, we provide a summary of the frequency of occurrence of solitary structures and of transverse hot tail formation. The region of decreasing occurrence of solitary structures early in the flight is apparently associated with the operation of the plasma source on the

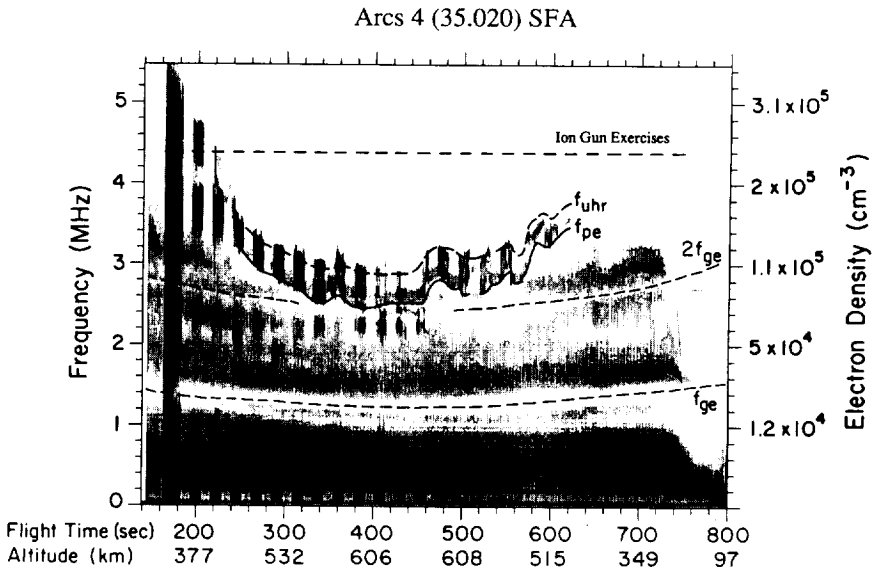

Figure 5. Spectrogram of high frequency electrostatic fluctuations observed at the ARCS4 main payload.

receding subpayload. Ion heating in this region is discussed by *Pollock et al.* [1992, 1995]. The second region of solitary structures occurred poleward of the main auroral arc and was accompanied by a similar increase in the occurrence of transverse hot tails, as seen by the HEEPS. The hot tails are always observed exclusively near 90° pitch angle. They are not observed when solitary structures are absent from the dc electric field data. The difference between the number of tails and the number of solitary structures per 5-s period stems from the fact that the latter are monitored continuously, whereas the first can only be diagnosed once per energy sweep of the HEEPS detector. Owing to that sweep, it is possible for short lived hot tails to go undetected.

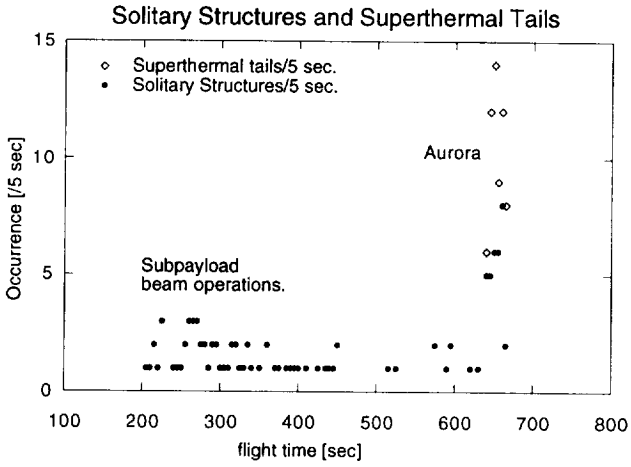

Figure 6. Association between dc electric field solitary structures and HEEPS observations of transverse tail heating events in the ions. The number of identifiable events per 5 s of time is plotted on the vertical axis. A tail event is identifiable if it produces counts in energy channels that are not excited by purely thermal plasma. A solitary structure is identifiable if a bipolar change of slope in the DCE interprobe potential is large enough to momentarily reverse the normal sinusoidal trend, so the detection threshold is reduced near the limits of the sinusoid.

Analysis

Payload Potential

A very important issue in the analysis of the plasma data from ARCS-4 is the accurate determination of the floating potential of the payload relative to the ambient plasma. The measured energies of the ions must be mapped to their external energies in the ambient plasma according to the relationship:

$$E_0 = E_m + eV_{s/c} \tag{1}$$

where E_0 is the external energy, E_m is the measured energy, e is the electron charge, and $V_{s/c}$ is the spacecraft floating potential relative to the plasma. For negative floating potentials, ions from the ambient plasma cannot have measured energies less than the energy corresponding to falling through the payload potential. For an RPA, this leads to a plateau on the retarding potential curve, but for a differential analyzer, the count rate will drop toward low energies below the floating potential with a form which is given by the step function response of the energy analyzer. The location of this edge can be used as a measure of the floating potential for purposes of mapping the observed energies to external energies. A suitable form of the data for determining the location of this edge is given in the Figure 1 spectrograms, where the data arrays have been summed across all azimuths and pitch angles, providing an angle-averaged measure of the lowest energy cutoff present in the entire angular distribution. The estimated position of the low energy edge at the floating potential may be visualized in Figure 1 as the low-energy boundary of the energy spectrogram.

Since the low-energy cutoff of the STICS sensor is not sharp, the following method was used to locate the effective "edge" of the response. The angle-averaged flux as a function of energy was differentiated, and the energy of maximal slope was determined. In general, it is easily shown that the convolution of a step function (a model for the true flux energy distribution in the vicinity of the low energy cutoff) and a single-humped response function, reaches maximum slope as the peak of the response function is at the position of the step function edge.

Therefore this energy is attributed to the presence of an equal negative floating potential, according to (1).

One check on the inference of payload floating potential from the lower edge of the count rate distributions was performed as follows. We assume that any feature which appears in association with the lowest-energy steps sampled, that is, colocated with the payload frame of reference in velocity space at all angles, must be produced by floating potential effects. Such features can be made apparent by plotting two-dimensional slices of the full three-dimensional distribution. The data was checked to be sure that such payload-frame features do not appear in the distribution functions derived using the floating potential measure described above.

A second check was performed by selecting data intervals that have nearly Maxwellian velocity distributions, as judged by fitting energy sweeps selected near the ram direction and fitting them with a "shifted, drifted Maxwellian" function (see Figure 13 below and associated discussion for examples). Convergence of the fitting process was robust, with fitting uncertainties in the parameters (N_i, $V_{s/c}$, E_{drift}, and kT_i) of the order of 10% or less. The inferred floating potentials agree with those derived from the approach described above with an error no larger that that associated with the width of the energy response (±11%). It can easily be appreciated that this uncertainty translates directly to a corresponding uncertainty in the temperature of the 3D distribution function (width of the energy distribution) for low Mach number species, and to a corresponding uncertainty in the flow energy of higher Mach number species (where the core is well displaced from the spacecraft frame). Other errors in this technique are second order and quite small.

Three-Dimensional Velocity Distributions

The raw count rates from STICS are converted directly into ion phase space densities using a knowedge of the calibration factors as shown in Table 1 (and their energy and angle dependences; not

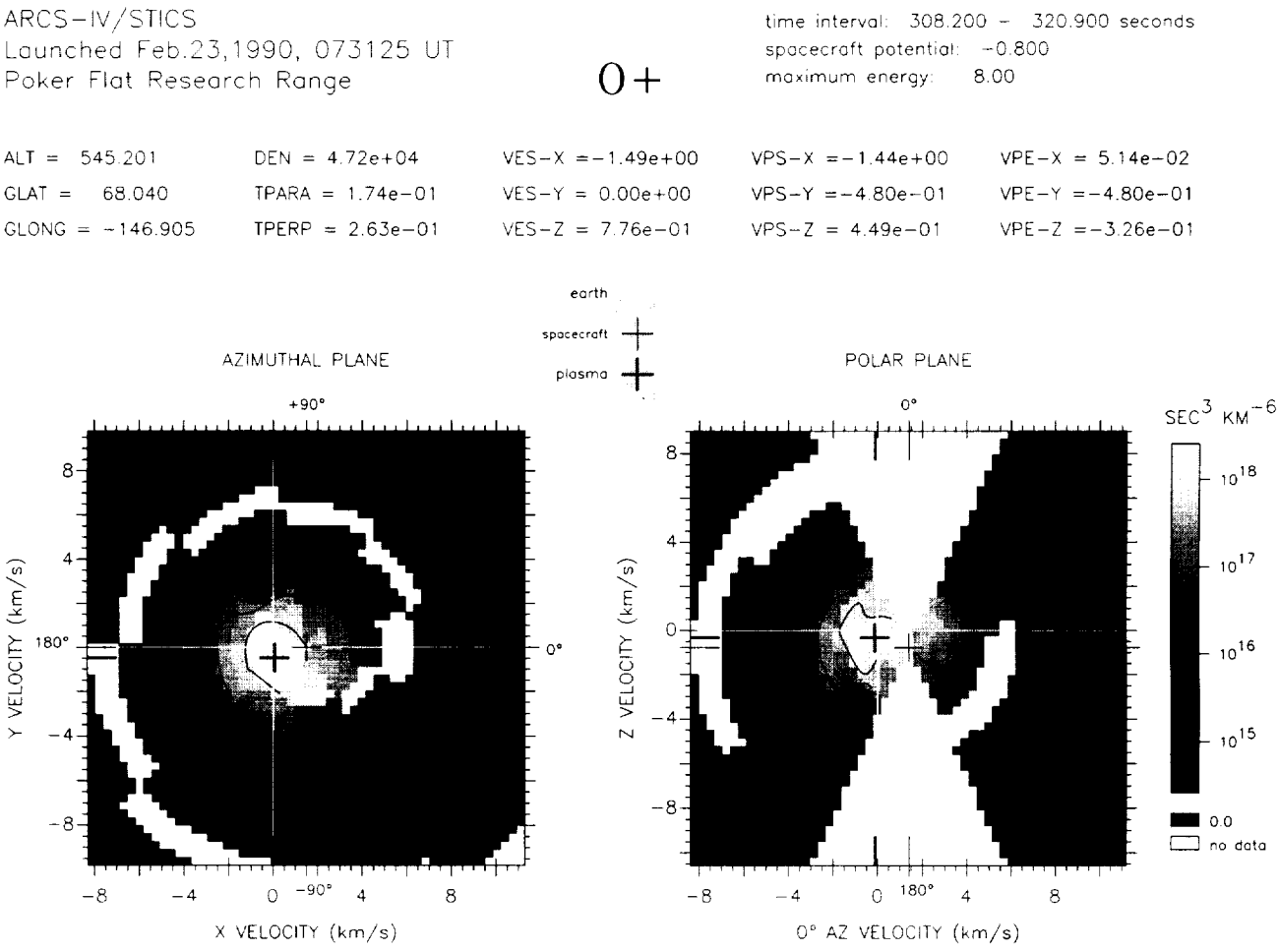

Figure 7. Three-dimensional representation of the O^+ velocity distribution for the period near 310 s. TAL of the ARCS-4 flight. The axes scale velocities relative to the Earth. Each data point is represented by a contoured value of the phase space density, arrayed in two panels representing cuts through the full velocity distribution in the plane perpendicular to the local magnetic field (left), and in a plane containing the local magnetic field (right). The bin structure contains 8 azimuths, 15 pitch angles, and 27 energies/speeds (radius). The azimuth of the cut in the right hand panel is indicated as 0°. The moments of the distribution are tabulated in the header documentation; velocities indicated include V_{ps} (plasma relative to spacecraft), V_{es} (Earth relative to spacecraft), and V_{pe} (plasma relative to Earth). A legend given at center indicates the crosshairs that mark the origins of the various coordinate systems: earth frame, spacecraft frame, and plasma frame.

shown here), and of the spacecraft floating potential, as described in the previous section (see also the appendix). Because the phase space density is constant along the trajectory of a particle, the phase space densities observed at the instrument aperture are equal to the phase space densities in the ambient medium. However, the velocity measured at the aperture must be mapped to the corresponding velocity in the external medium using the floating potential. Since the floating potential of a spacecraft in the ionosphere is generally negative, all ions are measured to have energies higher than their original energy in the ambient medium, and an apparent void in phase space is created at the lowest energies (i.e., the origin in the velocity frame of the payload), where no particles are present. This apparent void is removed by the mapping of observed energies to energies which are lower by the (negative) floating potential.

Figure 7 shows a double contour plot representation of the full three-dimensional distribution function for O^+ at a flight time well away from the main auroral arc. The two panels show the phase space densities in two orthogonal planes which cut the distribution perpendicular (left panel) and parallel (right panel) to the local magnetic field direction. The right panel vertical axis is *Vz*. The horizontal (transverse) axis cuts the distribution through the indicated azimuth in the coordinate system described above. The best estimate of the floating potential has been taken to be 0.8 V negative, based on the maximum slope of the low-energy flux cutoff. The value of phase space density corresponding to each energy step greater than 0.8 eV has been contoured according to the legend at the right, in a pixel placed at the velocity corresponding to the inferred external energy of ions. Regions of velocity space that have not been sampled (primarily the cones near the spin axis in the right panel, and a strip that spirals into the s/c frame origin in the left panel), are coded with a with a pattern that appears in the legend as "no data."

Once the floating potential is determined, it is relatively straightforward (see appendix) to compute the standard velocity moments of the distribution function (density, flow velocity, temperature, etc.), and these are tabulated on the figure along with other header documentation. To ensure that the computed moments do not suffer errors caused by the unsampled regions of velocity space, an iterative interpolation scheme is used to generate plausible estimates of the unsampled points using the sampled points as a guide (see appendix for details). The first velocity moments or flow components are indicated by crosshairs in the proper relationship to other crosshairs indicating the frame of the payload and the frame of the Earth. The velocity scales have their origins in coincidence with the Earth frame for convenience of interpretation. The distribution shown in Figure 7 is very nearly Maxwellian, except for an enhancement of phase space density found for perpendicular velocities in the distribution tail (right panel, along the 0° Az velocity scale).

Figure 8 shows the O^+ distribution for a later time interval during the passage of the payload over the auroral arc, in the

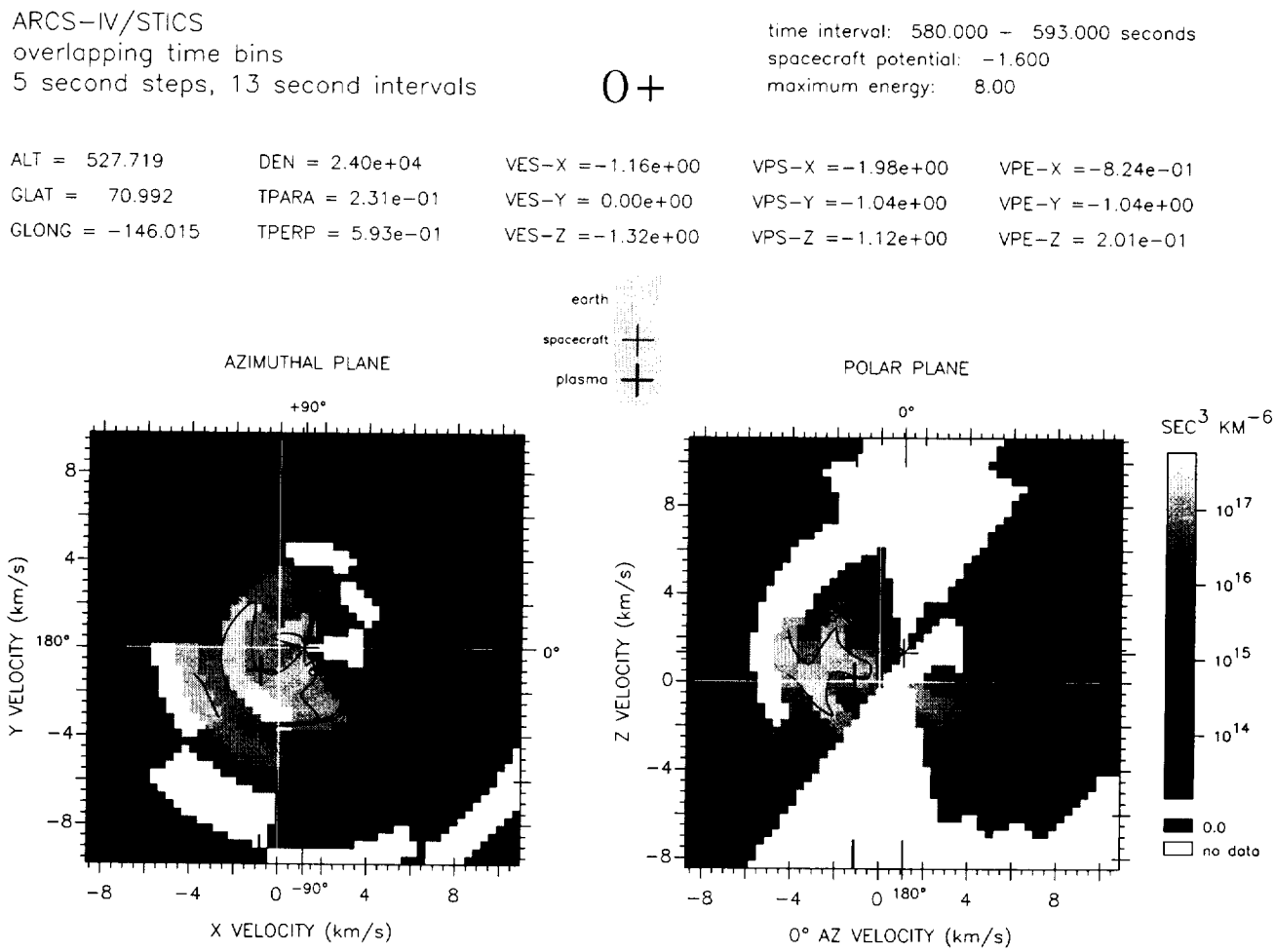

Figure 8. Similar to Figure 7., but giving the O^+ velocity distribution for the period near 585 s. TAL, as the payload entered the main auroral arc.

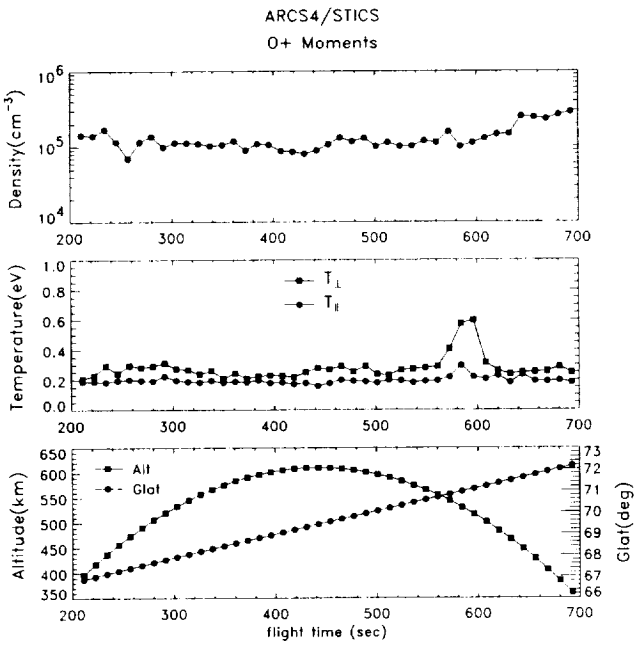

Figure 9. Selected velocity distribution moments for O^+ at the ARCS-4 main payload, throughout the flight. The bottom panel shows the payload position in altitude and geographic latitude during the flight.

same format as in Figure 7. Comparison with Figure 7 shows that a more extensive region of velocity space is occupied by the distribution. The moments, tabulated in the header, indicate a perpendicular temperature approximately a factor of two higher than in Figure 7, whereas the parallel temperature is approximately 35% higher than that of Figure 7.

Closer inspection of Figure 8 shows that the distribution is distinctly non-Maxwellian. The left panel (perpendicular velocities) reveals a large flat plateau centered on the bold crosshair representing the centroid of the plasma distribution. Still closer inspection of the phase space density contours shows that the ridge of maximum phase space density wraps around the lower side of that crosshair, nearly forming a closed minimum region. This is also confirmed by comparison with the right-hand panel (parallel and ram plane), which clearly shows a peak with lower phase space densities at lower perpendicular speeds, and makes it possible to visualize a cross section which is "ring" shaped. However, it must be borne in mind that the accumulation of this distribution spanned some 12 s, or 12 km of displacement perpendicular to the magnetic field. We return to the issue of data aliasing below.

Moment Parameters

In Figures 9 and 10 are plotted the time series of density and temperature moments calculated from the ARCS-4/STICS ion data, using the iterative interpolation scheme described in the Appendix. Beginning with the upper density plot panel of Figure 9, we see that the bulk of the flight data are from within the topside *F* region where O^+ densities fall with altitude. The scale height which gives the best exponential fit to the downleg topside O^+ data is slightly smaller than that inferred from the electron plasma frequency data, approximately 220 km. The minor ion species, H^+, He^+, and O^{++}, were each present at approximately the 1% level. As shown in Figure 10, H^+ and He^+ attained their maximum concentration near apogee. Though not shown in these figures, O^{++} was maximal near the *F* peak, similar to the O^+.

In the second panel from the top of Figure 9, we show the temperature results for O^+. Here it may be seen clearly that the auroral arc produces a significant enhancement of the O^+ temperature, from 2500 K to ~6000 K, but only in the perpendicular component. The corresponding panels of Figure 10 show the temperature variations of H^+ and He^+ ions. The notable increases of H^+ perpendicular temperature early in the flight were produced by operations of the Argon beam at 100 eV, and are the subject of another paper [Pollock et al., 1992, 1995]. There are clear increases of T_{perp} for both He^+ and H^+ in connection with the main auroral arc, similar in magnitude to but less localized than for O^+. It is interesting that both H^+ and He^+ show significantly enhanced perpendicular temperatures (relative to parallel temperature) throughout most of the flight except at low altitudes on the downleg, where the light ion temperatures were nearer to isotropy. This effect is not specifically associated with the auroral arcs, and as such is beyond the scope of the present paper. It was not observed during the late downleg when the payload passed through the main part of the *F* region, and it thought to represent a widespread dissipation of plasma wave energy in the light ion population. It can be noted that much of the perpendicular temperature enhancement is in the form of warm tail distributions transverse to the magnetic field.

The mean flow component moments are shown in Figure 11 in comparison with the ***ExB*** velocity components derived from the dc electric field measurements. The vertical or *Z* velocity (positive parallel to *B*, i.e. downward) may be seen to be small during the segment of the flight prior to crossing the main auroral

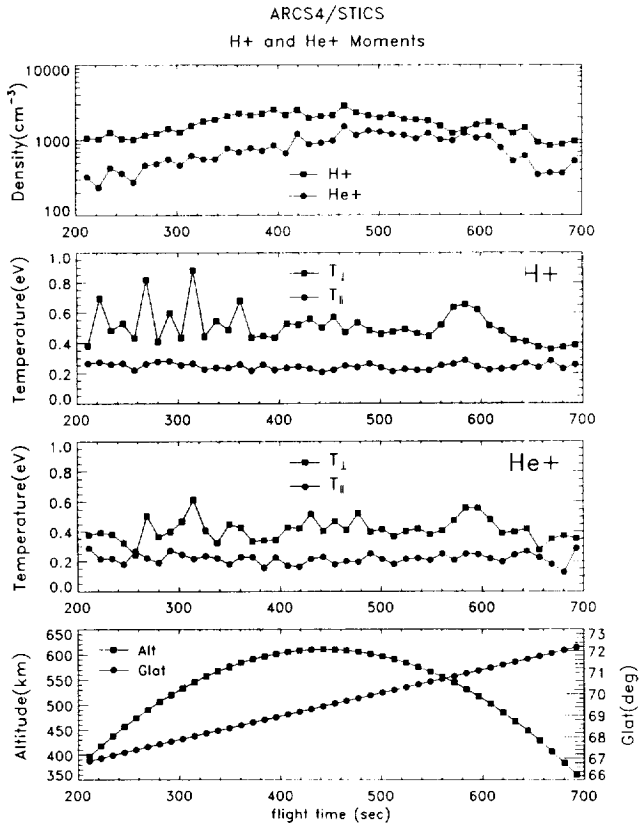

Figure 10. Similar to Figure 9., showing selected velocity distribution moments for H^+ and He^+ during the ARCS4 flight.

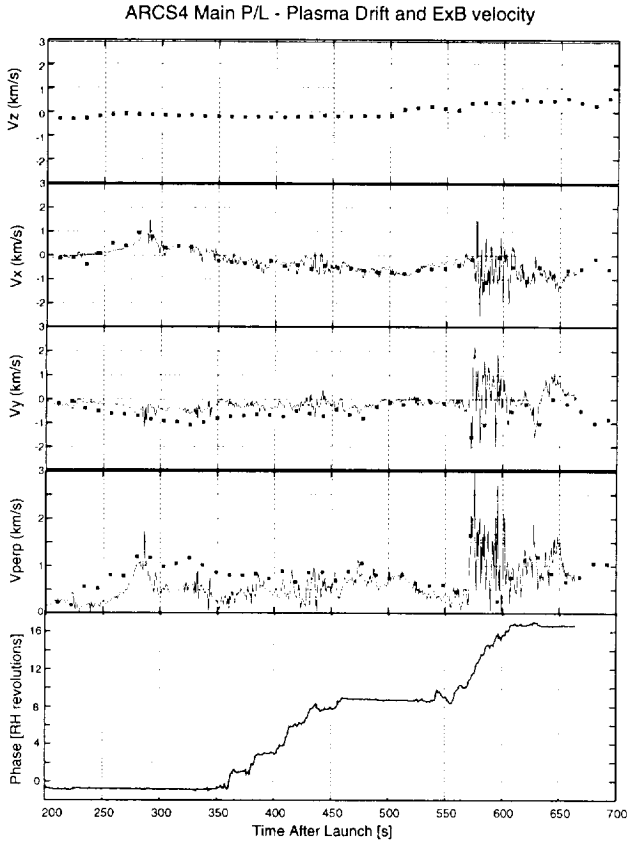

Figure 11. The three dimensional plasma drift inferred from STICS O^+ measurements (squares) and the field-perpendicular plasma drift inferred from the dc electric field (lines), measured at ARCS-4, expressed in the Earth frame of reference using the coordinate system described in the text, in which Z is parallel to the local magnetic field (downward), X lies in the trajectory plane directed northward, and Y is perpendicular to the X and Z, toward the east. The bottom panel shows the phase in revolutions of the perpendicular drift from the electric field components.

arc, which marks a transition to generally downward (positive V_Z) flow of up to and over 1 km/s. The poleward or X component of flow is essentially zero early in the flight, but then acquires a significant negative (equatorward, i.e., headwind) value as the payload progresses poleward through the main arc. There is one large poleward excursion of the plasma flow, exceeding the payload velocity, near 280-290 s TAL, and there are large fluctuations within the main auroral arc. The eastward or Y component of the flow is persistently negative equatorward of the arc, with a spike above 1 km/s in the same direction inside the main arc.

These general flow features are familiar from other measurements of plasma flows in the auroral zones and polar caps. In particular, a general downwelling throughout the nightside polar cap has been reported from DE 2 ion drift meter (IDM) work [*Lorance et al.*, 1990; *Heelis et al.*, 1992] and at higher altitudes from DE 1/RIMS work [*Moore et al.*, 1986b,c; *Chandler*, 1995]. Downward flows were also reported based on TOPAZ-2 rocket observations by *Garbe et al.*, [1992]. The poleward auroral arc has been found to be characterized by strong cross flows, even on a statistical basis [*Wu and Killeen*, 1992].

Corresponding first velocity moment (mean flow) data from H^+ and He^+ are characterized by error bars comparable with the observed flows, owing to their relatively large thermal speeds and consequent small flow Mach numbers, combined with relatively low counting rates as minor components of the plasma (see appendix for additional discussion). For example, typical H^+ thermal speeds are of the order of 8 to 10 km s^{-1}, with count rates leading to uncertainties in the first velocity moments, or flow, on the order of a few kilometers per second, rendering it impossible to measure drifts as small as a few hundred meters per second. Consequently, the O^+ data provide the most definitive measurement of plasma flow.

Electric Field and Plasma Convection

Sinusoidal fits to overlapping sets of 125 samples (fitting period of ~1.0 s or 0.6 spin period) of difference potential have been used to derive two components of the perpendicular electric field at a time resolution of 0.5 s (0.3 spin period). This procedure essentially assumes that the electric field is constant over the 0.5-s period and seeks the best approximation to this assumption, by treating finer scale variations as unresolved fluctuations. These electric field data provide an independent measure of the plasma drift velocity that is directly comparable to the plasma drift information derived from the STICS data. Again, two completely independent vector electric field solutions have been developed and reconciled to validate the results. Only minor quantitative differences between the two solutions exist, that apparently result from the slight differences in fitting procedures.

Figure 11 compares the plasma flow velocity as determined from the electric field ($\boldsymbol{E}\times\boldsymbol{B}/B^2$) with that derived from the plasma distribution functions. The top three panels show the "vertical" field-aligned drift (available only from the plasma), and the X and Y components in the coordinate system described above.The comparison indicates good agreement between the two in the ionospheric regions outside the auroral arc. It can be seen that the plasma flow increased within the auroral arc to values several times larger than its value in the adjacent, aurorally-inactive ionosphere, when computed in the Earth frame. Moreover, the plasma drift underwent very large amplitude oscillations with a period of ~ 4 s as the payload traversed the arc.

The nature of these oscillations is clarified somewhat by the lower two panels of Figure 11, which show the magnitude of the transverse flow velocity and the "phase" of the transverse flow velocity. This phase is the angle between the "detrended" flow vector and the X or poleward direction, expressed in revolutions. The detrending used here was the removal of a 5 s. running average flow from the 0.5-s flow velocity values. When a point-to-point change in the flow vector direction was found to be larger than 180°, it was assumed to have been a wrap around of the vector's rotation. When these "wraps" of the rotation were removed from the data set, the largest point-to-point change in the direction was found to be 160 deg. Therefore the wraparound data points were clearly distinguished from the balance of the data points, with the result that the vast majority of wraparounds were in the same direction, leading to an accumulating phase.

A striking contrast exists between the periods when the payload was within an auroral arc as compared with periods when it was between arcs. In particular, the passages through auroral arcs are marked by a steady increase in the phase of the plasma convective flow. Within the variable arc system encountered from 350 to 450 s TAL, a series of step-like

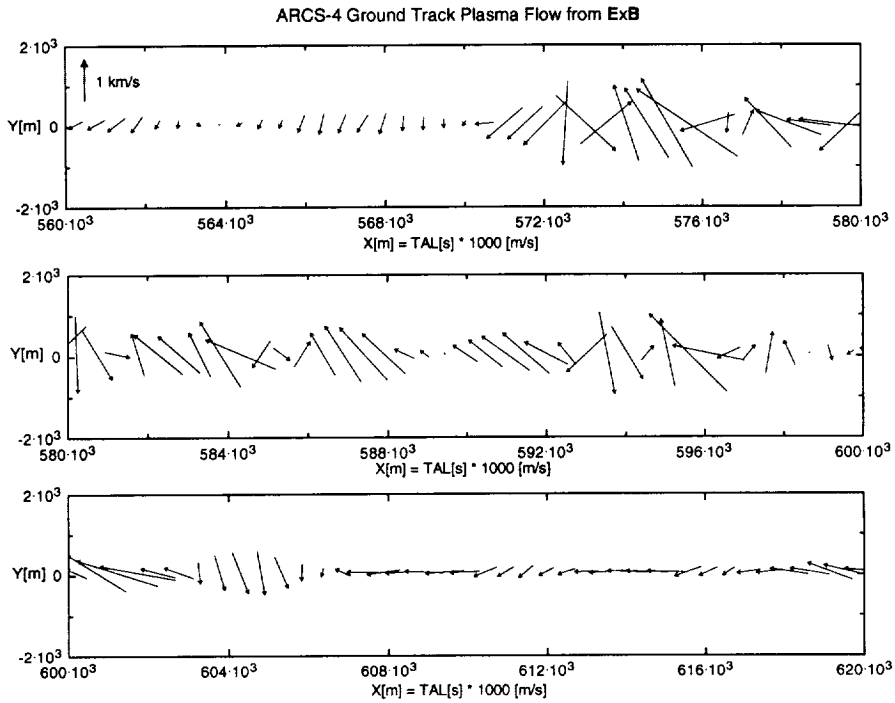

Figure 12. Presentation of the $\boldsymbol{E}\times\boldsymbol{B}$-derived plasma flow vector as a spatially varying flow field in the region spanning the main auroral arc form. The ground track distance is shown as a constant velocity multiplied by the time after launch, each vector measurement separated by a time of 0.5 s from its predecessor. The velocity vector scaling is such that each vector, drawn with its center at the point best characterizing the measurement, represents the distance traveled by the plasma in one second.

increases of phase can be discerned, each of roughly 2 revolutions. Within the steady main arc encountered from 570 to 605 s TAL, a more monotonic increase is seen, of roughly 8 revolutions. It was found that the flow rotations in the earlier set of arcs was dependent upon the detrending described above, and is not apparent if the flow velocity is expressed in the Earth frame. However, the rotations of the flow vector within the main arc system are nearly independent of the detrending procedure. This means that the flow rotation is dominant over the mean drift for this arc.

To further clarify the flow behavior, Figure 12 shows the $\boldsymbol{E}\times\boldsymbol{B}$ flow vector time series as the spatial series of flow vectors along the spacecraft ground track, for a period spanning the main arc. The general features of the flow can be visualized more easily in Figure 12, which clearly shows the rotation of the flow vector at a rate that varies greatly throughout the passage over the auroral arc.

For the periods within the auroral arc, double-probe electric field observations have at times been questioned on the grounds that significant probe-payload potentials may be produced by the energetic electron environment of the auroral arc. If the secondary emission characteristics of the probe differ from those of the payload, or when the probe is shadowed by the payload, it is certainly true that significant probe-payload potentials arise under electron bombardment. However, this will only produce a spurious difference signal if the secondary electron emission properties of the probes are significantly different from each other. Every effort was made to insure that the probes were identical. Moreover, the DCE signal exhibits a clean and coherent modulation phase behavior that is totally inconsistent with a spin modulation effect. Taken together, these multiple factors assure that the electric field can be regarded as giving a meaningful view of the large and variable plasma drifts.

The plasma drift and electric field data exhibited in Figures 11 and 12 indicate an extremely complex plasma flow environment within the auroral arc. With significantly lower time resolution, the direct plasma flow data only hint at this complexity and do not record drifts with magnitudes as large as those derived from the electric field data. Nevertheless, the fact that the plasma data also exhibit large and variable drifts within the arc validates the inference of large drifts from the electric field data.

Aliasing by Flow Variations

It is apparent from the results presented above that the three-dimensional plasma velocity moments presented above, based on count rate data accumulated over ~12 s of flight time, are aliased within the auroral arc where superthermal (for the O^+) plasma drifts vary strongly over times as short as a few seconds. Depending on the luck of the draw with respect to the phasing of the flow variations and the azimuth sampling (the dimension of slowest sampling), various outcomes are possible ranging from completely missing the core of the distribution, to accidentally seeing it in two or more azimuth sectors. In the latter case a relatively cold core could mistakenly be attributed with a higher temperature or a nonthermal shape. Evidently, our three-dimensional temperature moments are susceptible to errors resulting from the time aliasing of the data. Errors of this nature would be expected to elevate the apparent temperature relative to that of a true instantaneous distribution.

To address this and test the accuracy of the O^+ plasma temperature enhancements measured within the auroral arc, we

have examined our two-dimensional data (energy-pitch angle) to derive ion temperatures at higher time resolution within the auroral arc. Each three-dimensional distribution function as described above consists of eight two-dimensional measurements of the velocity distribution, sampling a corresponding number of azimuthal sectors at 1.5-s spacing in time. Owing to the broad exponential energy sweep (0.5 to 200 eV), the thermal peak of the distribution (1 to 5 eV) is swept out in approximately one fourth of this time, ~0.4 s. Thus each two-dimensional distribution permits measurement of the plasma temperatures at a temporal resolution of ~0.4 s, on 1.5-s centers.

To derive measurements of the temperature from individual energy-angle sweeps, we have first selected only the samples taken close to perpendicular to the magnetic field (60° to 120° pitch angle). We then have examined sweeps from each azimuth sampling. Figure 13 shows the results in three panels. The upper panel shows a series of perpendicular energy sweeps, one from each full three-dimensional data set, selected for high inferred temperature and spanning the entire crossing of the main auroral arc. In each case the data points have been fit with a simple Maxwellian model with the following parameters: 1) a normalization factor, 2) the spacecraft floating potential $V_{S/C}$, 3) the line-of-sight drift energy E_d, and 4) the thermal energy kT. The model also includes a simple model of the broadening of the low energy cutoff at the energy corresponding to the floating potential, an exponential tail having a width equal the measured energy passband of the electrostatic analyzer ($\Delta E/E$ = 0.22), referenced to the spacecraft potential. The fitting parameters are indicated in the legend of the figure. It is notable that the distributions at 544.9 s and 618.6 s, both outside the main auroral arc region, contain clear superthermal tails that stand above the fit curves. These seem to be a pervasive feature of the auroral ionosphere. While it is apparent that the plasma temperature rises and then falls in this series of fits, similar to the moment results, this impression is somewhat distorted by the selection of sweep data.

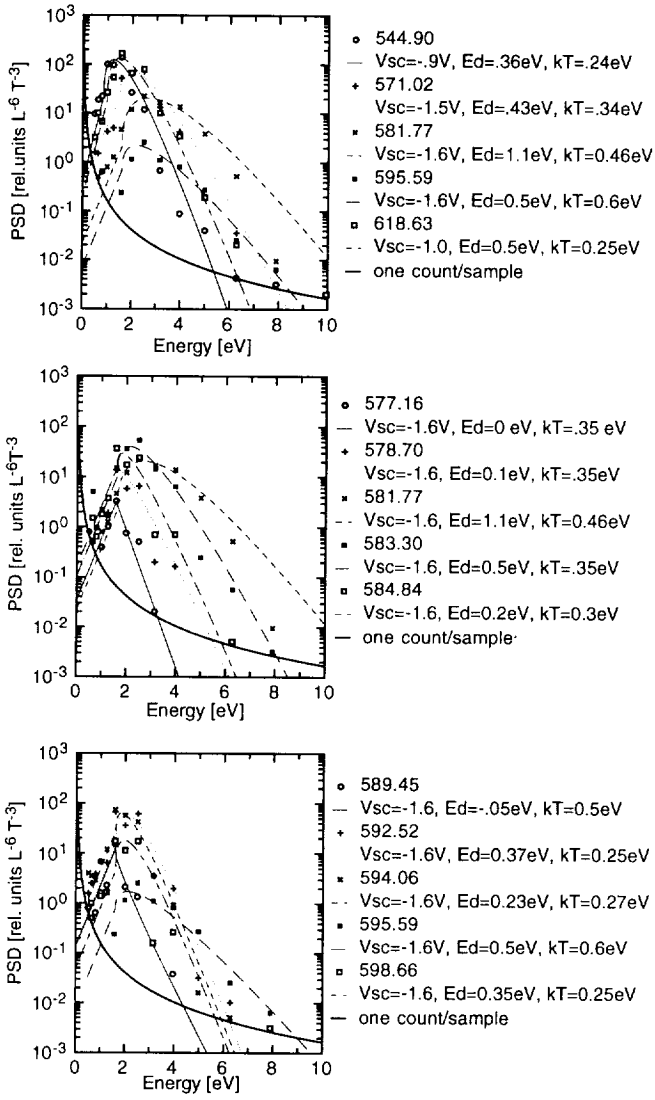

Figure 13. Selected perpendicular energy distributions representing 0.4-s snapshots of the O^+ data. (top) The warmest distributions for each three dimensional data set in a series that spans the entire bright auroral arc. (middle) Selection of distributions around 581.77 s TAL. (bottom) Selection of distributions around 595.59 s TAL.

In the center panel, we show a group of sweeps near in time to that beginning at 581.8 s TAL. The fit to the sweep beginning at 581.8 s fails to track the data points well at low or high energy, though it does a reasonable job in the immediate vicinity of the peak. This reflects a distribution that is significantly wider than is reflected in the slope of its wings. That is, it has a relatively flat top that cannot be well fit over the entire energy range with a Maxwellian. It can be seen that the fit shown overshoots the high energy tail, indicating that the fit overestimates the tail temperature. The fit is a least-squares compromise between errors in the high energy tail and in the low energy part of the distribution, and can be improved in one range only at the expense of the other. In such a case, the "mean random energy" returned by the moment approach is a more meaningful measure of temperature than the Maxwellian fit temperature. This nonthermal distribution may been considerably shorter lived than the three-dimensional data accumulation period of 12 s, so the moment result may not be representative of conditions throughout that interval. However, it does appear that the moment data provide a meaningful temperature (interpreted as "mean random energy") for the nonthermal distribution observed in this interval.

In the lower panel, we show a group of sweeps near in time to 595.6 s TAL. Here it can be seen that the elevated temperature seen at that time is really not representative of the core of the distribution seen at nearby azimuths, and could be better characterized as a warm tail distribution, present throughout this period. In fact, the core itself appears to be quite cool during this period within the auroral arc. Further evidence for a warm tail is seen in the fit to the distribution at 589.5 s, where the negative drift energy fit parameter indicates these are wake observations with the core largely shifted out of view by the plasma relative wind. These results confirm that the moments results are indeed aliased by the large drift fluctuations during the 590-600 s period. In this more poleward part of the arc, the core is relatively cold but there is a warm tail present that contributes to elevated moment temperatures, and it seems likely that variations of the plasma drift lead to an apparent broadening of the core in the three-dimensional distribution moment results, leading to artificially large temperatures in that period. The highest core distribution temperatures attained in O^+ during this interval were on the order of 0.3 eV, rather than 0.6 to 0.7 eV as indicated by the moments.

Discussion

Superthermal Frictional Heating

Frictional heating of both ions and neutrals occurs whenever the ionospheric plasma is caused to flow relative to the embedded neutral gas by coupled magnetospheric motions. In the event that such motions exceed the thermal speed, the formation of an ion velocity distribution shaped like a ring centered on the plasma drift velocity has been predicted [e.g., *St.-Maurice and Schunk*, 1979]. Owing to the presence of a strong magnetic field in this ionospheric context, it is problematic to refer to such high speed flows as supersonic (the MHD fast mode speed is much larger than the thermal speed). For this reason, we refer to frictional heating in this high speed regime as "superthermal". Some previous observations from strongly drifting ionospheric regions have been interpreted in terms of such a toroidal distribution function [*St.-Maurice et al.*, 1976; *Lockwood et al.*, 1987].

Figure 14 schematically illustrates the mechanism whereby superthermal ion drift in an auroral arc results in the ring- or toroidal-shaped distribution approximately centered on the bulk plasma drift velocity in velocity space. The basic process is a frictional interaction between the magnetospheric plasma distributed along the entire auroral arc field line, including the ionospheric plasma, and the neutral atmosphere in which the latter is embedded. The patterned circle at the center of the plot represents the Maxwellian velocity distribution of the neutral gas. The crosshair along the negative X axis is the location of a hypothetical perpendicular drift of plasma relative to the neutrals. It is assumed that the ions collide with neutrals and have their velocities randomized isotropically in the neutral frame, with a collision period which is long compared with a gyroperiod. It is further assumed that ion-ion collisions are much less frequent than ion-neutral collisions.

The result is that after collisions with the neutrals (mainly resonant charge exchange for O^+ in O, but also scattering collisions for O^+ in N_2), ions appear near the origin, within the neutral atom velocity distribution, and are subsequently accelerated by the $-\boldsymbol{V}x\boldsymbol{B}$ electric field, executing gyro motions that in velocity space are circles centered on the plasma-neutral drift velocity. Each ion makes several transits around the gyro orbit before suffering another collision with the neutrals in which a new slow ion is produced, assuming a small, randomly directed velocity prior to being again picked up the convective electric field. Clearly, if the drift speed is larger than the neutral thermal speed, an ion distribution which has a minimum near the drift velocity will be formed, absent other processes that might thermalize this distribution. This feature is strongest when resonant charge exchange dominates over scattering collisions.

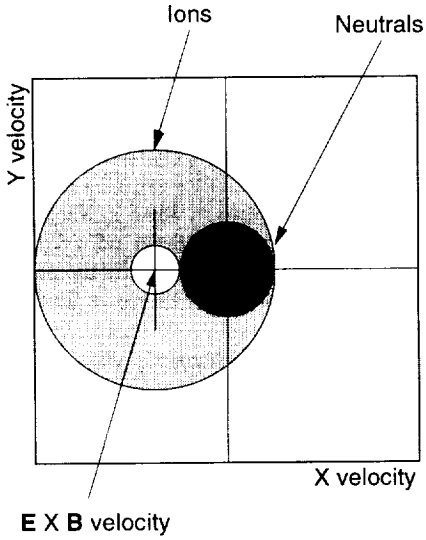

Figure 14. Schematic illustration of the formation of toroidal or ring beam distributions in the topside ionosphere.

One of the other processes which can intervene is ion-ion self-collisions. The distribution of collision frequencies is such that ion-ion collisions tend to become more important relative to ion-neutral collisions and charge exchange, with increasing altitude in the F region. *Kinzelin and Hubert* [1992], consider this phenomenon at altitudes as high as 600 km, where the ARCS-4 payload traveled. It was found that the toroidal or ring feature persists at such altitudes, but that a stronger drift is required to produce the feature than at lower altitudes nearer the F peak.

The assumptions of the "standard" theories are beginning to be relaxed. For example, *St.-Maurice et al.*[1994] have considered the situation in the presence of flow shear. Their results imply that the shears observed by us are far too small to make any significant difference from the uniform flow case. Given significant vertical flows, not seen in the auroral context reported here, complex nonlocal effects would need to be considered, as for example they were by *Lorance and St.-Maurice* [1994] and by *Wilson* [1994]. Upflows, for example, can extend the vertical altitude range within which a toroidal distribution could be observable.

The observations reported here are the first of which we are aware with the capability to resolve the three-dimensional structure of a ring in velocity space at ionospheric energies. Unfortunately, a convincing demonstration of this capability in a real ionospheric situation has been frustratingly eluded by the rapid variability of the plasma environment. The electric field observations demonstrate the existence of conditions suitable for nonthermal frictional heating, but also tell us that the superthermal plasma winds were very rapidly varying in space and/or time, inconsistent with the assumptions of current theories of the formation of ring distributions. Thus they have provided crucial information that prevents us from taking the apparent ring shape too literally, while alerting us to the complexity of the actual situation in this auroral heating event. If we seek to test in more detail the theory of superthermal frictional heating, the challenge is clearly to improve the temporal resolution of the plasma instrumentation so that a three-dimensional distribution function can be resolved in ≤ 1 s, that is, in a half spin of a typical rocket payload.

Though the direct evidence for a toroidal velocity distribution is somewhat marginal here, there is good evidence for superthermal frictional heating. If we correlate the perpendicular ion flow velocities with the O^+ temperatures using the functional form used by *Winkler et al.* [1992], we find the result shown in Figure 15. There is considerable scatter in the data, probably owing to the unresolved variability in the plasma flows as well as the unknown neutral winds, with correlation coefficients (R) for the fits ~0.5-0.6. Nevertheless, the best fit coefficients ($\beta_{/\!/}$ and $\beta_\perp$ of *Winkler et al.* [1992]) are in reasonable agreement with results presented by *Winkler et al.* [1992] for cases with mainly O background gas and small concentrations of N_2. The inferred neutral temperature is a bit higher than typical, but this may be consistent with the auroral energy dissipation present. The $\beta_{/\!/}$ value is a bit higher, and $\beta_\perp$ is a bit lower than might be expected, but these expectations are somewhat dependent on

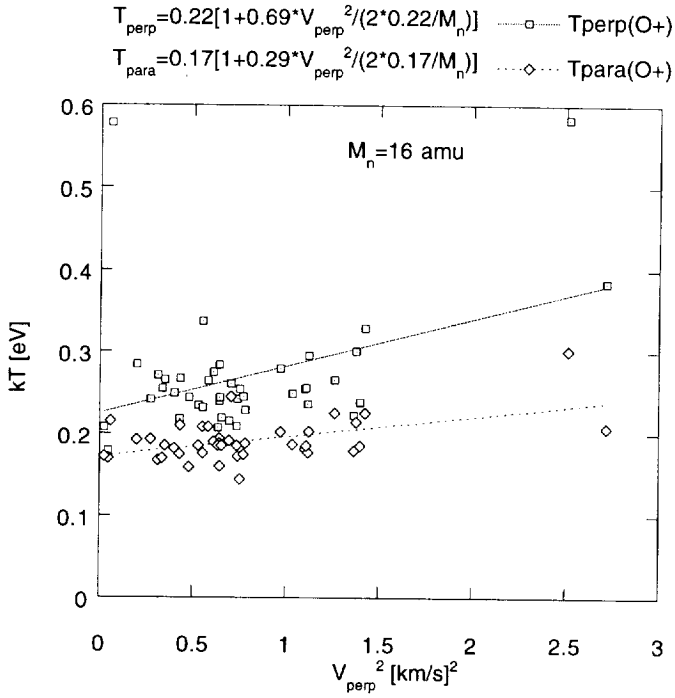

Figure 15. Comparison of the O^+ temperature results with the perpendicular flow results. Both parallel and perpendicular temperatures are correlated with the perpendicular flow as shown. Best fit parameters are shown in the equations for the fit lines. The correlation coefficients (R) for the fits are 0.55 for the T_{perp} fit (excluding the two high temperature points) and 0.51 for the T_{parl} fit.

neutral composition. Considering the scatter in the data, it may be a bit presumptuous to attempt to infer neutral composition from this measurement. Nevetheless, the general ionospheric situation can be characterized as being in quantitative agreement with the expectations of frictional heating theory.

Two data points stand out from the grouping around the frictional heating fit in Figure 15, corresponding to the highest O^+ temperatures within the auroral arc. However, we have shown above that, in one case, the temperatures derived from the moments are artifactually elevated by aliasing of the three-dimensional data by drift variations, in the poleward part of the arc, where the plasma drift was quite small (Figure 11). If the lower temperature inferred from the fits of Figure 14 were substituted for this point in Figure 15, only a single point would remain outside the frictional heating grouping. The remaining standout point is the one that applies to the nonthermal distribution of figures 8 and 13. This distribution, too, might be attributable to the very large spike of plasma drift, to 3 km/s, that occurred shortly before it was observed, as seen in Figure 11.

However, there is also significant heating of the light ions, where the ion Mach number is a factor of 4 lower for He^+ and a factor of 16 lower for H^+, yet similar temperature enhancements are recorded in these species within the auroral arc. The low ion Mach number for the light ions also reduces the apparent temperature increase from aliasing by drift fluctuations, by a similar factor. While frictional heating is clearly observed in the O^+ plasma, frictional heating alone does not account for the presence of warm O^+ tails nor the observed heating of the light ion species, which similarly contains both core heating and warm tail components.

Shear-Driven Heating

The large amplitude oscillation of the drift and DCE means either that plasma convection within the auroral arc was strongly structured with a scale of approximately 2-4 km (in view of the transverse velocity of the payload ~1 km/s), or that the convection in the arc was subject to a very large amplitude hydrodynamic wave structure with a corresponding period. Others have recorded similar convective behavior within auroral arcs, an earlier example being *Kelley and Carlson* [1977]. Observing the magnetic field as well as the electric field, *Boehm et al.* [1990] reported examples of similar observations that in certain cases did and in other cases did not exhibit correlated magnetic perturbations with magnitudes characteristic of hydromagnetic waves. More recently, *Earle et al.* [1989] have drawn attention to the correlation between comparable rates of shear and associated higher frequency turbulence in the auroral ionosphere. It appears that this and other auroral arcs are at times highly structured as sheets of opposite drift, with correspondingly large shear rates between them (4 km/s in $\geq$ 2 km or $\leq$ 2 Hz, or 0.05 when normalized to the local O^+ cyclotron frequency), or that the auroral ionosphere is subject to large-amplitude Alfvèn waves with similar rates of "shear."

A related heating mechanism may be relevant to the auroral situation reported here, based on the very large observed rates of shear in the superthermal plasma drifts. This is the shear driven instability of Ganguli et al. [1994]. In addition to providing conditions ripe for superthermal frictional heating, the sharp structuring of the strong drifts observed in the ARCS-4 dc electric field provides appropriate conditions for shear driven wave instability and resultant heating. Shear heating is a form of anomalous perpendicular viscosity that arises from an ion cyclotron wave instability in configuration space. The normalized shear rates reported here are on the order of 0.05, which appears to be submarginal to excite this instability. Ganguli et al. [1994] argued using simulation techniques that structures with smaller

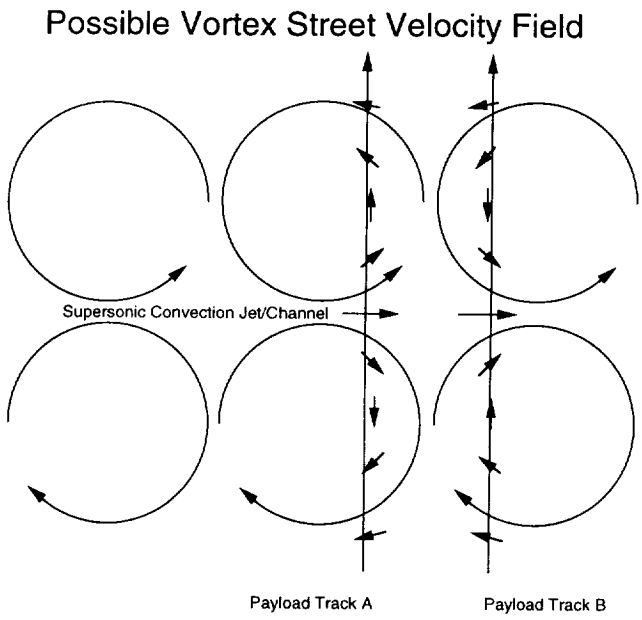

Figure 16. Schematic illustration of the apparent rotation of the transverse flow vector along hypothetical payload tracks across the array of vortex streets associated with an intense flow channel.

rates of shear can evolve through a cascade to smaller scales and increasing shear rates, ultimately triggering the shear instability as the dissipation mechanism.

The simulations of *Ganguli et al.* [1994] also indicate the formation of vortexes having a spatial flow structure somewhat similar to that which we infer from the DCE phase observations, described above. It is well-established through imagery from auroral low-light level TV [e.g., *Wescott et al.*, 1993] that active auroral arcs contain numerous vortex-like features having associated brightness, and presumeably current, enhancements. In Figure 16, we have illustrated schematically the flow characteristics of the twin vortex street associated with an intense flow channel. Also indicated in Figure 16 is the qualitative flow signature that would be observed by a diagnostic payload crossing the structure along two different tracks that produce opposite apparent rotations of the flow vector. On the basis of this interpretation of the data, it is possible that the present observations are indicative of vortical motions within an auroral arc. With published auroral imagery and the simulations of Ganguli, our observations lead toward a plausibility argument for an auroral heating mechanism based on dissipation of flow shear energy that leads to multiple rows of vortices as well as smaller scale dissipative structures. However, quantitative comparison with our light ion temperatures is beyond the scope of the present paper.

Core and Tail Heating

Here we have reported core and tail heating within a bright and relatively steady nightside auroral arc, producing temperatures a factor of order 2-3 above that of the surrounding ionosphere in the light ions, and in both core and tail of the O^+. The heating was apparently insufficient or of too short duration to create a strongly upwelling region but appears to have stopped and turned around the downward flow of the polar cap plasma convecting into the arc. In addition to the core heating observed in this auroral arc, ARCS-4 also recorded the occurrence of numerous solitary structure events that were associated with sporadic tail heating of the ambient ion population. The two phenomena were apparently quite independent of each other, the solitary structures and tail heating occurring mainly outside the auroral arc and strong plasma drift features. Further analysis of the tail heating is beyond the scope of the present paper, in which the focus is on the bulk plasma flow and core heating.

Plasma Instability

Several authors have noted that the ring-shaped nonthermal ion distribution function should be unstable to perpendicularly propagating waves which would tend to thermalize the energy associated with gyration around the plasma drift speed [*Post and Rosenbluth*, 1966; *Ott and Farley*, 1975; *Lakhina and Bhatia*, 1984]. On the other hand, it has been pointed out, based on linear dispersion theory [*St.-Maurice*, 1978], that Landau damping of the same waves into parallel electron heating may nullify the ion wave growth rate and thereby preserve the unstable ring feature. One might expect that parallel electron heating would be observed when such Landau damping is significant; however, this is a somewhat open issue which depends on a nonlinear treatment for its resolution. The low frequency wave and electron environments are clearly important in understanding the situation within the auroral topside ionosphere.

The ARCS-4 data set provides some relevant evidence. The waves produced by the operation of a plasma source on the remote subpayload were sufficiently intense at the main payload to hamper observation of the natural lower hybrid wave environment, because the automatic gain control of the receiver was not able to recover quickly enough between firings of the plasma source to make quantitative measurements of the ambient waves levels. Consequently, it is not possible to clearly identify a LHR enhancement associated with the main auroral arc. However, low-energy field-aligned electron enhancements are apparent and very well correlated with the auroral activity. It is known that isotropic low-energy electron enhancements are produced by backscatter and secondary emission due to incident auroral primary electrons [e.g., *Evans*, 1974] and field aligned enhancements of electron fluxes are often associated with dynamic auroral forms [*Arnoldy et al.*, 1985], so this evidence must be evaluated carefully. Backscatter and secondary electrons are quite isotropic in contrast with Landau heated electrons that should be field-aligned. Owing to detector saturation of angular imaging, it cannot be said if field alignment was or was not present in the lowest-energy measured electron fluxes (~50 eV). However, the electrons in the 200 eV and higher-energy ranges were not affected by imaging saturation and were definitely field-aligned. The electron fluxes shown in Figure 3 are downcoming parallel fluxes. Upgoing fluxes were not sampled but could have been present at the same times. The enhancement of parallel low energy electron flux was present throughout the auroral arc, not solely associated with its edges. It therefore appears clear that these electrons represent a hot parallel tail on the thermal electron core. However, more definitive thermal and superthermal electron observations will be needed to fully specify the electron distribution related to this kind of plasma heating.

Conclusions

Three-dimensional core and tail plasma observations have been made at altitudes from 250 to 620 km, passing poleward over a stable evening auroral arc between 550 and 500 km altitude at the poleward edge of the auroral oval.

The payload encountered a variable (including a negative excursion), and then increasing plasma headwind from the polar cap, at speeds of order 1 km s^{-1}. O^+ vertical bulk flow velocity was small equatorward of and within the arc and downward within the polar cap poleward of the arc. There was evidence that a downward flow at $\geq$ 1 km s^{-1} in the polar cap was slowed and reversed as the plasma flowed generally equatorward across the arc heating region.

Superthermal and highly variable plasma winds were encountered as the payload passed through the auroral arc, consistent either with passage of the payload through a series of vortex structures or through a broader scale, circularly polarized hydromagnetic wave structure. Drift measurements were obtained by dc electric field measurements at a time resolution of ~0.5 s and were highly variable with a timescale of ~4 s, and reached instantaneous amplitudes of up to 3 km s^{-1}. On the basis of DCE measurements, the rate of shear in the structured plasma flow reached values of a few Hertz or $\leq$ 0.05 normalized to the local O^+ gyrofrequency.

Anisotropic core plasma heating was observed with peak perpendicular temperatures of 0.4-0.5 eV in the O^+, 0.5-0.6 eV in the He^+, and 0.6-0.7 eV in the H^+ ions, to be compared with ambient ionospheric temperatures of 0.2-0.3 eV in the majority O^+. The O^+ distribution was apparently ring or toroid shaped in three-dimensional (12 s) data at one point within the arc, with its center approximately at the bulk perpendicular drift speed and its

edge passing through the neutral gas (Earth) velocity frame. This is the signature expected for superthermal frictional heating, but is ambiguous owing to the severe aliasing of the plasma measurements by the rapid drift velocity variations. The same distribution was clearly nonthermal when examined in two-dimensional (0.4 s) energy-angle data. The O^+ heating was consistent with the expectations of frictional heating theory within the broad ionospheric context of this flight including evidence for a nonthermal core within the superthermal drifts of the auroral arc. However, there were warm tails in the O^+, and the auroral core and tail heating of the light ion species was well beyond the expectations of frictional heating. It seems plausible but cannot be conclusively shown in this case that the dynamic auroral environment included a wave environment responsible for the additional ion heating.

Evidence for the plasma/collective effects of superthermal frictional heating predicted by linear theory was suggestive but somewhat ambiguous. Low-energy electron heating to 100s of eV was observed and was demonstrably field parallel as expected for Landau damping of the predicted waves. Localized lower hybrid waves predicted to be most unstable by linear dispersion theory could not be identified clearly owing to the operation of a plasma source on a remote subpayload. Fluctuations in the heavy ion cyclotron frequency range were observed but distinct enhancements of these latter waves were most closely associated with the solitary structure events and sporadic tail heating, rather than with the large plasma drifts and bulk heating.

Appendix: Moments and Uncertainties

Computation of the velocity distribution moments presented in this paper was performed according to the equations and procedures given below. Schematically, the raw count rates are converted to phase space densities using the instrument response parameters given in Table 1 to compute differential, directional fluxes, which are then converted to phase space densities using the particle speed at the instrument aperture.

$$f = \frac{R[Hz]}{\delta A(\theta', E') \cdot \delta\Omega(\theta', E') \cdot \delta E(\theta', E')} \cdot \left(\frac{m}{v'^2}\right) \quad (2)$$

Here f is the conventional phase space density, the denominator factors are the energy and angle-dependent response sensitivities of the STICS sensor as given in Table 1, and the factor in parentheses is the Jacobian relating the volume element in energy-angle space to the volume element in phase space. The primed quantities refer to values as measured at the instrument aperture. The result is an array of $f(i,j,k)$, and associated arrays specifying the sample coordinates associated with the indices: energies $E'(i)$, pitch angles $\theta'(j)$, and azimuths $\phi'(k)$.

The external velocity coordinates associated with each phase space density data point are computed in accord with the spacecraft floating potential computed as described in the main text. The moment calculations are then direct sums over the external energies and angles, as detailed below:

Density:

$$\begin{aligned} n &= \iiint f v^2 dv \sin(\theta) d\theta d\phi \\ &= \sum f v^2 \delta v \sin(\theta) \delta\theta \delta\phi \\ &= \sum f \frac{v}{m} \delta E \sin(\theta) \delta\theta \delta\phi \end{aligned} \quad (3)$$

Velocity (three components):

$$\begin{aligned} V_i &= \iiint f v_i v^2 dv \sin(\theta) d\theta d\phi \\ &= \sum f v \cos(\phi) \sin(\theta) v^2 dv \sin(\theta) d\theta d\phi \\ &= \sum f \frac{v^2}{m} \delta E \cos(\phi) \sin^2(\theta) d\theta d\phi \end{aligned} \quad (4)$$

Temperature plus flow energy (three components, of which two are degenerate perpendicular temperatures):

$$\begin{aligned} V_i^2 &= \iiint f v_i^2 v^2 dv \sin(\theta) d\theta d\phi \\ &= \sum f v^2 \cos^2(\phi) \sin^2(\theta) v^2 dv \sin(\theta) d\theta d\phi \\ &= \sum f \frac{v^3}{m} dE \cos^2(\phi) \sin^3(\theta) d\theta d\phi \end{aligned} \quad (5)$$

The resulting moments suffer from errors in the basic data values, as well as errors due to unsampled regions of velocity space, which can only be corrected by interpolating the surrounding data into the unsampled regions. The unsampled regions are of two types: First, the sampling strategy used during ARCS-4 resulted in occasional unsampled energy/azimuthal "pixels," owing to the nonintegral number of instrument sweeps in a spin-sweep beat period. This effect can be readily identified in Figures 7 and 8. These missing data lead to varying errors in the moments, which are particularly serious when the missing data pixel intersects the regions of maximum phase space density. Second, the axial blind spots (small and large pitch angles) are similarly unsampled, leading to errors in the moments, especially during periods of rapid upward or downward motion (along the magnetic field), as seen in the payload frame of reference.

These problems were addressed by means of an "iterative interpolation" scheme that is equivalent in some ways to the more traditional method of fitting data to plausible distributions with free parameters. Moments were computed from the valid data points, without any attempt to fill the missing data values. These moments were then used to specify a bi-Maxwellian distribution, from which were drawn estimates of the phase space density for each unmeasured point. These estimates were treated as estimates of phase space density in the unsampled regions of velocity space, and new moments were then computed by integrating over both the original data points (which are never changed) and the estimated values. This entire process was then iterated, with each new set of moments being used to specify a revised bimaxwellian estimate of the phase space density at the unsampled points. When correctly applied, this procedure was found to converge rapidly, within several iterations, leading to results as plotted in Figures 9-11.

Uncertainties in computed moments are estimated by propagating the errors associated with the individual measurements, mainly absolute calibration uncertainty (20%) and Poisson counting uncertainties ($\sqrt{n}$). The fractional error in the density moments owing to counting statistics is approximately equal to the fractional error of the highest phase space density in the distribution ($\sqrt{n}/n$). The errors in the mean flow moments can be shown to be essentially equal to this ratio multiplied by the thermal speed of the distribution. For the O^+ data shown here, the peak count samples were $\leq 10^3$ counts, so the uncertainty ratio above was approximately 3%. Applied to a thermal speed comparable with the flow speeds, this gives good accuracy for

the flow speeds. For the light/minor ion data, the samples peaked at ≤ 30 counts, so the uncertainty ratio was ~20%. Given that the light ion thermal speed exceeds the flows by a factor around 4-8, this kind of uncertainty makes the light ion mean flow velocity moments relatively useless as mean flow measurements.

Uncertainty owing to unsampled points and the iterative interpolation method is believed to be increased by the factor N_{tot}/N_{meas}, where N_{tot} is the total number of nonzero points used to compute the moment, and N_{meas} is the number of them that were actually measured, or less than 1.40 for the data sets used here.

Acknowledgments. D. L. Reasoner contributed fundamentally through all phases of the development of the STICS instrument and this paper is dedicated to his memory. W. L Chisholm was responsible for the overall system engineering of STICS. The STICS electrostatic optics were raytraced and optimized by V. N. Coffey of MSFC and M. A. Sloan of Computer Sciences Corp. The STICS sequencer and low voltage power supplies were developed by J. Currie, C. Oliver, and P. Smith of the MSFC Astrionics Laboratory. Its magnetic mass analyzer and stepping power supplies were developed by J. H. Hoffman, W. W. Wright, and D. Tipton of the University of Texas at Dallas. V. N. Coffey performed flight calibration. A. Kelley and D. England supported its development and launch. Development of the UNH HEEPS instruments was engineered by M. Widholm and M. Lessard. Development of the Cornell DC/VLF electric field instrument was engineered by S. Powell. This work was supported by the OSSA Space Physics Division, Ionospheric Physics Branch, Suborbital Program, under UPNs 442-36 and 435-11 at MSFC, under grants NAG6-12 and NAG5-692 at the University of NH, and under grants NAG5-601 and NAG5-691 at Cornell University.

The editor thanks J.J. Berthelier and J-P. St.-Maruice for their assistance in evaluating this paper.

References

Arnoldy, R. L., T. E. Moore, and L. J. Cahill Jr., Low altitude field-aligned electrons, *J. Geophys. Res., 90*, 8445, 1985.

Arnoldy, R. L., K. A. Lynch, P. M. Kintner, J. Vago, S. Chesney, T. E. Moore, and C. J. Pollock, Bursts of transverse ion acceleration at rocket altitudes, *Geophys. Res. Lett., 19*, 413, 1992.

Barakat, A. R., R. W. Schunk, and J. P. St.-Maurice, Monte carlo calculations of the O+ velocity distribution in the auroral ionsphere, *J. Geophys. Res., 88*, 3237, 1983.

Basu, Su., S. Basu, E. MacKenzie, P. F. Fougere, W. R. Coley, N. C. Maynard, J. D. Winningham, M. Sugiura, W. B. Hanson, and W. R. Hoegy, Simultaneous density and electric field fluctuation associated with velocity shears in the auroral oval, *J. Geophys. Res., 93*, 115, 1988.

Boehm, M. H., C. W. Carlson, J. P. McFadden, J. H. Clemmons, and F. S. Mozer, High-resolution sounding rocket observations of large-amplitude Alfvén waves, *J. Geophys. Res., 95*, 12157, 1990.

Chandler, M. O., Observations of downward moving O^+ in the polar topside ionosphere, *J. Geophys. Res., 100*, p.5795, 1995.

Chang, T., and B. Coppi, Lower hybrid acceleration and ion evolution in the suprauroral region, *Geophys. Res. Lett., 8*, 1253, 1981.

Chang, T., G. B. Crew, N. Hershkowitz, J. R. Jasperse, J. M. Retterer, and J. D. Winningham, Transverse acceleration of oxygen ions by electromagnetic ion cyclotron resonance with broadband left-hand polarized waves, *Geophys. Res. Lett., 13*, 636, 1986.

Chappell, C. R., T. E. Moore, and J. H. Waite, Jr., The ionosphere as a fully adequate source of plasma for the Earth's magnetosphere, *J. Geophys. Res., 92*, 5896, 1987.

Crew, G. B., and T. Chang, Ion cyclotron resonance heated conics: theory and observations, *J. Geophys. Res., 95*, 3959, 1990.

Earle, G. D., M. C. Kelley, and G. Ganguli, Large velocity shears and associated electrostatic waves and turbulence in the auroral *F* region, *J. Geophys. Res., 94*, 15321, 1989.

Evans, D. S., Precipitating electron fluxes formed by a magnetic field-aligned potential difference, *J. Geophys. Res., 79, 2853*, 1974.

Ganguli, S. B., and P. J. Palmadesso, Plasma transport in the auroral return current region, *J. Geophys. Res., 92*, 8673, 1987.

Ganguli, G., M. J. Keskinen, H. Romero, R. Heelis, T. Moore, and C. Pollock, Coupling of microprocesses and macroprocesses due to velocity shear: An application to the low-altitude ionosphere, *J. Geophys. Res., 99*, 8873, 1994.

Garbe, G. P., R. L. Arnoldy, T. E. Moore, P. M. Kintner, and J. L. Vago, Observations of transverse ion acceleration in the topside auroral ionosphere, *J. Geophys. Res., 97*, 1257, 1992.

Heelis, R. A., W. R. Coley, M. Loranc, and M. R. Hairston, Three dimensional ionospheric circulation, *J. Geophys. Res., 97*, 13903, 1992.

Kelley, M. C., and C. W. Carlson, Observations of intense velocity shear and associated electrostatic waves near an auroral arc, *J. Geophys. Res., 82*, 2343, 1977.

Kintner, P.M., J. Vago, S. Chesney, R.L. Arnoldy, K.A. Lynch, C.J. Pollock, and T.E. Moore, Localized lower hybrid acceleration of ionospheric plasma, *Phys. Rev. Lett., 68*, 2448, 1992.

Kinzelin, E., and D. Hubert, Ion velocity distribution function in the upper auroral *F* region: 1. Phenomenological approach, *J. Geophys. Res., 97*, 4061, 1992.

Klumpar, D. M., Transversely accelerated ions: An ionospheric source of hot magnetospheric ions, *J. Geophys. Res., 84*, 4229, 1979.

Lakhina, G. S., and K. G. Bhatia, Ion cyclotron instability in the auroral *F* region, *J. Geophys. Res., 89*, 9845, 1984.

Lockwood, M., and T. J. Fuller-Rowell, The modeled occurence of non-thermal plasma in the ionosphere F-region and the possible consequences for ion outflows into the magnetosphere, *Geophys. Res. Lett., 14*, 371, 1987.

Lockwood, M., B. J. I. Bromage, R. B. Horne, J.-P. St.-Maurice, D. M. Willis, and S. W. H. Cowley, Non-maxwellian ion velocity distributions observed using EISCAT, *Geophys. Res. Lett., 14*, 111, 1987.

Loranc, M., R. A. Heelis, W. B. Hanson, and J.-P. St.-Maurice, A morphological study of vertical ionospheric flows in the high-latitude *F* region, *J. Geophys. Res., 96*, 3627, 1990.

Loranc, M. and J.-P. St.-Maurice, A time-dependent gyro-kinetic model of thermal ion upflows in the high-latitude *F* region, *J. Geophys. Res., 99*, p.17,429, 1994.

Lundin, R., and B. Hultqvist, Ionospheric plasma escape by high-altitude electric fields: magnetic moment "pumping", *J. Geophys. Res., 94*, 6665, 1989.

Lynch, K. A., R. L. Arnoldy, P. M. Kintner, and J. L. Vago, Electron distribution function behavior during localized transverse ion acceleration events in the topside auroral zone, *J. Geophys. Res., 99*, 2227, 1994.

Lysak, R. L., M. K. Hudson, and M. Temerin, Ion heating by strong electrostatic ion cyclotron turbulence, *J. Geophys. Res., 85*, p.678, 1980.

Maggs, J.E., Electrostatic noise generated by the auroral beam, *J. Geophys. Res., 83*, 3173, 1978.

Moore, T. E., C. J. Pollock, R. L. Arnoldy, and P. M. Kintner, Preferential O^+ Heating in the Topside Ionosphere, *Geophys. Res. Lett., 13*, 901, 1986a.

Moore, T. E., M. Lockwood, M. O. Chandler, J. H. Waite, Jr., C. R. Chappell, A. Persoon, and M. Sugiura, Upwelling O^+ ion source characteristics, *J. Geophys. Res., 91*, 7019, 1986b.

Moore, T. E., J. H. Waite Jr., M. Lockwood, and C. R. Chappell, Observations of coherent transverse ion acceleration, in *Ion Acceleration in the Magnetosphere and Ionosphere, Geophysical Monogr. Ser.*, vol. 38, edited by T. Chang , p. 50, AGU, Washington, D. C., 1986c.

Moore, T. E., Origins of Magnetospheric Plasma, *U.S. Natl. Rep. Int Union Geod. Geophys. 1987-1990, Rev. Geophys., 29*, 1039, 1991.

Newman, A. L., Thermal energization of ions during impulsive field events, *Geophys. Res. Lett., 17*, 1061, 1990.

Ott, E., and D. T. Farley, Microinstabilities and the production of short-

wavelength irregularities in the auroral *F* region, *J. Geophys. Res., 80*, 4599, 1975.

Pollock, C. J., M. O. Chandler, T. E. Moore, J. H. Waite Jr., C. R. Chappell and D. A. Gurnett, A survey of upwelling ion event characteristics, *J. Geophys. Res., 95*, 18969, 1990.

Pollock, C. J., T. E. Moore, R. L. Arnoldy, and P. M. Kintner, Preferential transverse heating of light ions during ionospheric Ar^+ beam injection experiment, *Eos Trans. AGU, 73, Fall Meet. Suppl.*, 218, 1992.

Pollock, C.J., M.O. Chandler, T.E. Moore, R. L. Arnoldy, P. M. Kintner, S. Chesney, and L. J. Cahill, Jr., Preferential heating of light ions during an ionospheric Ar^+ injection experiment, *J. Geophys. Res., 100*, 15477, 1995.

Post, R. F., and M. N. Rosenbluth, Electrostatic instabilities in finite mirror confined plasmas, *Phys. Fluids, 9*, 730, 1966.

Sharp, R. D., R. G. Johnson, and E. G. Shelley, Observation of an ionospheric acceleration mechanism producing energetic (keV) ions primarily normal to the geomagnetic field direction, *J. Geophys. Res., 82*, 3324, 1977.

St.-Maurice, J.-P., On a mechanism for the formation of VLF electrostatic emissions in the high latitude *F* region, *Planet. Space Sci., 26*, 801, 1978.

St.-Maurice, J.-P., and R. W. Schunk, Velocity distributions in the high latitude ionosphere, *Revs. Geophys., 17*, 1979.

St.-Maurice, J.-P., W. B. Hanson, and J. C. G. Walker, Retarding potential analyzer measurement of the effect of ion-neutral collisions on the velocity distribution in the auroral ionosphere, *J. Geophys. Res., 81*, 5438, 1976.

St.-Maurice, J.-P., E. Winkler, and A. M. Hamza, Ionospheric ion velocity distributions and associated transport properties in the presence of auroral electric field gradients, *J. Geophys. Res., 99*, 19527, 1994.

Tsunoda, R. T., R. C. Livingston, J. F. Vickrey, R. A. Heelis, W. B. Hanson, F. J. Rich, and P. F. Bythrow, Dayside observations of thermal ion upwellings at 800 km altitude: an ionospheric signature of the cleft ion fountain, *J. Geophys. Res., 94*, 15277, 1989.

Vago, J.L., P.M. Kintner, S.W. Chesney, R.L. Arnoldy, K.A. Lynch, T.E. Moore, and C.J. Pollock, Transverse ion acceleration by localized lower hybrid waves in the topside ionosphere, *J. Geophys. Res., 97*, 16395, 1992.

Wahlund, J.-E., and H. J. Opgenoorth, EISCAT observations of strong ion outflows from the F-region ionosphere during auroral activity: Preliminary results, *Geophys. Res. Lett., 16*, 727, 1989.

Wescott, E. M., T. J. Hallinan, H. C. Stenbaek-Nielsen, D. W. Swift, and D. D. Wallis, Rapid ray motions in barium plasma clouds and auroras, *J. Geophys. Res., 98*, 3711, 1993.

Whalen, B. A., W. Bernstein, and P. W. Daly, Low altitude acceleration of ionospheric ions, *Geophys. Res. Lett., 5*, 55, 1978.

Whealton, J. H., and S. B. Woo, Ion velocity distribution of a weakly ionized gas in a uniform electric field of arbitrary strength, *Phys. Rev. A, 6*, 2319, 1971.

Wilson, G. R., Kinetic modeling of O^+ upflows resulting from **ExB** convection heating in the high-latitude *F* region ionosphere, *J. Geophys. Res., 99*, 17453, 1994.

Winkler, E., J.-P. St.-Maurice, and A. R. Barakat, Results from improved Monte Carlo Calculations of auroral ion velocity distributions, *J. Geophys. Res., 97*, 8399, 1992.

Wu, Q., and T. L. Killeen, Statistical studies of thermosphere-ionosphere coupling in the vicinity of auroral arcs, *Eos Trans. AGU, 73, Fall Meet. Suppl.*, 226, 1992.

Yau, A. W., B. A. Whalen, A. G. McNamara, P. J. Kellogg, and W. Bernstein, Particle and wave observations of low-altitude ionospheric ion acceleration events, *J. Geophys. Res., 88*, 341, 1983.

Yau, A. W., and M. Lockwood, Observations of ionospheric outflows, in *Modeling Magnetospheric Plasma, Geophys. Monogr. Ser.*, vol. 44, edited by T.E. Moore and J.H. Waite Jr., p. 229, AGU, Washington, D. C., 1988.

R. L. Arnoldy, and B. Austin, Department of Physics, University of New Hampshire, Durham, NH 03824.

J. Bonnell and P. M. Kintner, School of Electrical Engineering, Cornell University, Ithaca, NY 14850.

M. O. Chandler, T. E. Moore, C. J. Pollock, Space Sciences Laboratory, Marshall Space Flight Center, Huntsville, AL 35812.

(Received January 23, 1995; revised October 10, 1995;
accepted October 11, 1995.)